The Abdus Salam
International Centre for Theoretical Physics

United Nations
Educational, Scientific and
Cultural Organization

IAEA
International Atomic Energy Agency

2168-1

Joint ICTP-IAEA Workshop on Dense Magnetized Plasma and Plasma Diagnostics

15 - 26 November 2010

The Plasma Focus-Scaling Properties to Scaling Laws

S. Lee and S.H. Saw
Institute for Plasma Focus Studies
Melbourne
Australia

The Plasma Focus- Scaling Properties to Scaling Laws

S Lee[1,2,3] and S H Saw[1,2]

[1]INTI International University, 71800 Nilai, Malaysia
[2] Institute for Plasma Focus Studies, 32 Oakpark Drive, Chadstone, VIC3148, Australia
[3] Nanyang Technological University, National Institute of Education, Singapore 637616
e-mails: leesing@optusnet.com.au; sorheoh.saw@newinti.edu.my

Abstract

Recent extensive and systematic numerical experiments have uncovered new insights into plasma focus devices including the following: (i) a plasma current limitation effect, as device static inductance L_0 is reduced towards very small values; (ii) scaling laws of neutron yield Y_n and soft x-ray yield Y_{sxr} as functions of storage energies E_0 and currents I; (iii) a global scaling law for neutron yield Y_n as a function of storage energy E_0 combining experimental and numerical data showing that scaling deterioration has probably been interpreted as neutron 'saturation'; and (iv) a fundamental cause of neutron 'saturation'. An important scaling property is that the plasma condition is the same whether the plasma focus is a small sub-kilojoule machine or a large one with thousands of kilojoules of stored energy; and the related constancy of the dynamic resistance. This scaling property turns out to be the cause of 'scaling deterioration' of yields. The understanding of this situation points to a new class of plasma focus devices to overcome the 'saturation' of I and yields. Plasma focus technology has to move to ultra-high voltage technology and take advantage of circuit manipulation techniques in order to move into a new era of high performance. This paper will examine fundamental scaling properties of the plasma focus including speeds and dynamic resistance, temperatures, dimensions and times, these being computed in the model which thus is a good source of reference for diagnostics. More importantly, we link up these basic scaling characteristics with the crucial ideas of the inherent yield scaling deterioration, thus providing a clear understanding of its overall performance characteristics, paving the way for future exploitation. The paper also takes a peek at the latest development of modeling the instability phase using anomalous resistance terms, resulting in quantitative experimental data of the instability phase of the plasma focus.

Keywords: Plasma Focus, Nuclear Fusion, Plasma Focus Scaling, Plasma Focus Properties, Neutron Saturation

1. Introduction

The plasma focus is one of the smaller scale devices which complements the international efforts to build a nuclear fusion reactor [1,2]. It is an important device for the generation of intense multi-radiation including x-rays, particle beams and fusion neutrons. The physics underlying the mechanisms for the generation of these radiations in the plasma focus is still not completely known although there have been intensive investigations for the past five decades. Experimental and theoretical work on the focus has reached quite high levels. For example, detailed simulation work on the plasma focus had been carried out since 1971 [3] and a large range of devices has been constructed from sub-kJ focus [4] to greater than 1 MJ large focus. Advanced experiments have been carried out on the dynamics, radiation, instabilities and non-linear phenomena [5]. Yet despite all these intensive studies, very little regarding scaling appears to be documented with the exception of the scaling law for neutron yield. Other more recent work has thrown much needed light on other aspects of scaling such as how the dimensions of the dense focused plasma (the focus pinch) and the pinch lifetime scale with apparatus dimensions, the dominating dimension being the anode radius [5-7].

2. Neutron scaling with energy

Historically the most appealing quantity for use as the base for scaling is the stored energy used to drive the focus. Using the highest voltage technologically convenient all one needs to do to scale up energy ($E_0=0.5C_0V_0^2$) is to put more capacitors in parallel, thus increasing the capacitance C_0 of the energy bank and incidentally also decreasing the static inductance L_0 of the bank to some extent. Along these lines, early work has shown that $Y_n\sim E_0^2$ [5,9]. Under ideal conditions (minimized inductance L_0 and when the system is dominated by the generator impedance) the capacitor current I may have the relationship $I\sim E^{0.5}$, then it quickly follows that $Y_n\sim I^4$. This very simplistic view has led to the hold-up of the progress of large plasma focus devices. It was found that when the capacitor bank reached storage energies of only several hundred kJ the neutron yield no longer increased; the so-called neutron saturation effect [5]. It has been shown recently that whilst the discharge circuit is indeed dominated by the generator impedance at low energies (i.e. low C_0) so that indeed $I\sim E^{0.5}$; at a certain point when the C_0 (i.e. E_0) gets sufficiently big, the generator impedance has dropped to such low values as to reach the value of the load impedance that the generator is driving. As E_0 is increased even further and further, the generator impedance eventually becomes negligible when compared to the load impedance which remains relatively constant, hardly affected by the decreasing generator impedance [10,11]. Eventually at very large E_0, the constant load impedance completely dominates and the circuit current reaches an asymptotic value and hardly increases for any further increase in E_0 at those already very large values. At this point which would be beyond the high tens of MJ for the plasma focus, the capacitor current may be considered to have saturated, leading to neutron saturation. What is observed at hundreds of kJ and which has been termed as neutron saturation is based on very limited data. When more data from more experiments are put together with data from rigorous systematic numerical experiments, then the global picture shows the scaling deterioration very clearly (see Figure 1) [11]. We will come back to this central problem again in the Section 9 of this paper.

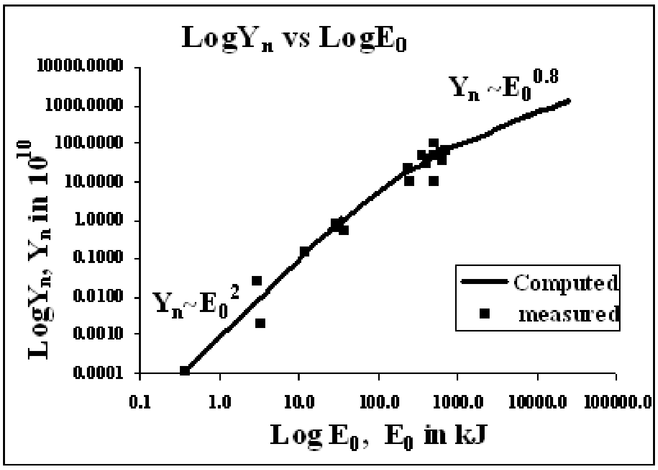

Figure 1. The global scaling law, combining experimental and numerical data. The global data illustrates Y_n scaling observed in numerical experiments from 0.4 kJ to 25 MJ (solid line) using the Lee model code, compared to measurements compiled from publications (squares) of various machines from 0.4 kJ to 1 MJ.

3. Scaling Properties of the Plasma Focus

3.1. Various Plasma Focus Devices

In Figure 2a is shown the UNU ICTP PFF 3 kJ device [12] mounted on a 1m by 1m by 0.5m trolley, which was wheeled around the ICTP for the 1991 and 1993 Plasma Physics Colleges. The single capacitor is seen in the picture mounted on the trolley. In contrast, Figure 2b shows the 300-times larger PF1000, the 1 MJ device at the ICDMP in Warsaw Poland [13]. Only the chamber and the cables connecting the plasma focus to the capacitors are shown. The capacitor bank with its 288 capacitors, switches and chargers are located in a separate hall.

Figure 2a. 3 kJ UNU ICTP PFF

Figure 2b. 1 MJ PF1000 plasma focus

In order to throw further light on aspects of scaling such as how the dimensions of the focused pinch and the pinch lifetime scale with apparatus dimensions we have compiled tables (see following two sections) from numerical experiments, involving small and large plasma focus devices with a view of finding the relationship among relevant scaling properties.

3.2. Scaling Properties: mainly axial phase and neutron yield

We show in Table 1 the characteristics of three plasma focus devices [12-16] computed using the Lee model code [14,16], fitted by comparing the computed current waveform to the measured current waveform. These computed characteristics are also in broad agreement with measured experimental values where available in the published literature [12-16].

Table 1.

	E_0	A	z_0	V_0	P_0	I_{peak}	v_a	ID	SF	Y_n
	kJ	cm	cm	kV	Torr	kA	cm/μs	kA/cm	(kA/cm) torr$^{0.5}$	10^8
PF1000	486	11.6	60	27	4	1850	11	160	85	1100
UNU ICTP	2.7	1.0	15.5	14	3	164	9	173	100	0.20
PF-400J	0.4	0.6	1.7	28	7	126	9	210	82	0.01

In Table 1 we look at the PF1000 and study its properties at typical operation with device storage at 500 kJ level. We compare this big focus with two small devices at the kJ and sub-kJ level.

We note:

Voltage and pressure do not have any particular relationship to E_0.
Peak current I_{peak} increases with E_0.
Anode radius 'a' increases with E_0.
Current per cm of anode radius (ID) I_{peak}/a is in a narrow range 160 to 210 kA/cm.
SF (speed or drive factor) $(I_{peak}/a)/P_0^{0.5}$ is 82 to 100 (kA/cm) torr$^{0.5}$ deuterium gas [6].
Peak axial speed v_a is in the narrow range 9 to 11 cm/us.
Fusion neutron yield Y_n ranges from 10^6 for the smallest device to 10^{11} for the PF1000.

We stress that whereas the ID and SF are practically constant at around 180 kA/cm and 90 (kA/cm) per torr$^{0.5}$ deuterium gas throughout the range of small to big devices, Y_n changes over 5 orders of magnitude.

We emphasize that the data of Table 1 is generated from numerical experiments and most of the data has been confirmed by actual experimental measurements and observation.

3.3. Scaling Properties: mainly radial phase and focus pinch

Table 2.

	c= b/a	a	T_{pinch}	v_p	r_{min}	z_{max}	Pinch duration	r_{min}/a	z_{max}/a	Pinch duration/a
		cm	10^6K	cm/μs	cm	cm	ns			ns/cm
PF1000	1.4	11.6	2	13	2.2	19	165	0.17	1.6	14
UNU ICTP PFF	3.4	1.0	8	26	0.13	1.4	7.3	0.14	1.4	8
PF400J	2.6	0.6	6	23	0.09	0.8	5.2	0.14	1.4	9

Table 2 compares further the properties of the range of plasma focus devices. The properties compared in this table are mainly related to the radial phase. These are computed from numerical experiments and found to be in close agreement with laboratory measurements [12-16].

We note:

Pinch temperature T_{pinch} is strongly correlated to the square of the radial pinch speed v_p.
v_p itself is closely correlated to the value of v_a and c=b/a; so that for a constant v_a, v_p is almost proportional to the value of c=b/a [14,16].
Dimensions and lifetime of the focus pinch scales as the anode radius 'a':
r_{min}/a (almost constant at 0.14-0.17)
z_{max}/a (almost constant at 1.5)
Pinch duration has a relatively narrow range of 8-14 ns/cm of anode radius.
Duration per unit anode radius is correlated to the inverse of T_{pinch}.

T_{pinch} itself is a measure of the energy per unit mass. It is quite remarkable that this energy density at the focus pinch varies so little (factor of 4) over a range of device energy of more than 3 orders of magnitude (factor of 1000).

This practically constant pinch energy density (per unit mass) is related to the constancy of the axial speed moderated by the effect of the values of c=b/a on the radial speed.

The constancy of r_{min}/a suggests that the devices also produce the same compression of ambient density to maximum pinch density; with the ratio (maximum pinch density)/(ambient density) being proportional to $(a/r_{min})^2$. So for two devices of different sizes starting with the same ambient fill density, the maximum pinch density would be the same.

3.4. Scaling Properties: Rules- of- Thumb

From the above discussions, we may put down as rule-of-thumb the following scaling relationships, subject to minor variations caused primarily by the variation in c=b/a.

Axial phase energy density (per unit mass)	constant
Radial phase energy density (per unit mass)	constant
Pinch radius ratio	constant
Pinch length ratio	constant
Pinch duration per unit anode radius	constant
Dynamic resistance, axial phase	constant

Summarising, the dense hot plasma pinch of a small E_0 plasma focus and that of a big E_0 plasma focus have essentially the same energy density [6-8], the same mass density. The big E_0 plasma focus has a bigger physical size and a bigger discharge current. The size of the plasma pinch scales proportionately to the current and to the anode radius, as does the duration of the plasma pinch. The bigger E_0, the bigger I_{peak}, the bigger 'a' has to be, correspondingly the larger the plasma pinch radius and the longer the duration of the plasma pinch. The larger size and longer duration of the big E_0 plasma pinch are essentially the properties leading to the bigger neutron yield compared to the yield of the small E_0 plasma focus. We have also included that the axial phase dynamic resistance is a constant as a rule-of thumb. This is related to the constant axial phase energy density but is listed here as it plays a predominant role in the physical mechanism of deterioration of yield scaling which will be discussed in greater detail in Section 9.2.

3.5. Dimensions and Lifetimes of the plasma focus in D and Ne

We may also summarise the dimensions and lifetimes for deuterium and neon plasma focus pinch as follows [7,8]:

Table 3.

		Deuterium	**Neon (for SXR)**
minimum radius	r_{min}	0.15a	0.05a
max length (hollow anode)	Z	1.5a	1.6a
radial shock transit	t_{comp}	5×10^{-6}a	4×10^{-6}a
pinch lifetime	t_p	10^{-6}a	10^{-6}a
Speed factor	SF	90	

Where, for the times in sec, the value of anode radius, a, is in m. For the neon calculations radiative terms are included; and the stronger compression (smaller radius) is due to thermodynamic effects. The units of the speed factor SF are: (kA/cm)/(torr$^{0.5}$)

The above description of the plasma focus combines data from numerical experiments using the Lee Model code, consistent with laboratory observations [6-8,14,16].
The next section describes briefly the code.

4. Introduction to the Lee model code

The Lee model code couples the electrical circuit with plasma focus dynamics, thermodynamics, and radiation, enabling a realistic simulation of all gross focus properties. The basic model, described in 1984 [17], was successfully used to assist several projects [12,18,19]. Radiation-coupled dynamics was included in the five-phase code, leading to numerical experiments on radiation cooling [20]. The vital role of a finite small disturbance speed discussed by Potter in a *Z*-pinch situation [21] was incorporated together with real gas thermodynamics and radiation-yield terms. This version of the code assisted other research projects [22-27] and was web published in 2000 [28] and 2005 [29]. Plasma self-absorption was included in 2007 [28], improving the SXR yield simulation. The code has been used extensively in several machines including UNU/ICTP PFF [12,14,16,20,22,24-27,30], NX2 [23,31,32], and NX1 [32,33] and has been adapted for the Filippov-type plasma focus DENA [34]. A recent development is the inclusion of the neutron yield Y_n using a beam–target mechanism [10,11,35-39], incorporated in recent versions [14,16] of the code (versions later than RADPFV5.13), resulting in realistic Y_n scaling with I_{pinch} [10,11,35-38]. The versatility and utility of the model are demonstrated in its clear distinction of I_{pinch} from I_{peak} [36,37] and the recent uncovering of a plasma focus pinch current limitation effect [37-40], as static inductance is reduced towards small values. Extensive numerical experiments had been carried out systematically resulting in the uncovering of neutron [1,10,11,35,41-43,48] and SXR [41-48] scaling laws over a wider range of energies and currents than attempted before. The numerical experiments also gave insight into the nature and cause of 'neutron saturation' [1,10,11,42]. The description, theory, code, and a broad range of results of this "Universal Plasma Focus Laboratory Facility" are available for download from [14,16].
A brief description of the 5-phase model is given in the following.

4.1. The 5-phases

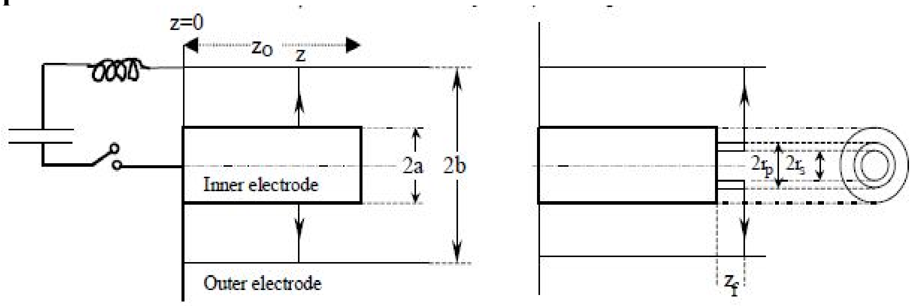

Figure 3. Schematic of the axial and radial phases. The left section depicts the axial phase, the right section the radial phase. In the left section, z is the effective position of the current sheath-shock front structure. In the right section r_s is the position of the inward moving shock front driven by the piston at position r_p. Between r_s and r_p is the radially imploding slug, elongating with a length z_f. The capacitor, static inductance and switch powering the plasma focus are shown for the axial phase schematic only.

The five phases (*a-e*) are summarised [14,16, 35-49] as follows:
a. Axial Phase (see Figure 3 left part): Described by a snowplow model with an equation of motion which is coupled to a circuit equation. The equation of motion incorporates the axial phase model parameters: mass and current factors f_m and f_c [18,50]. The mass swept-up factor f_m accounts for not only the porosity of the current sheet but also for the inclination of the moving current sheet-shock front structure, boundary layer effects, and all other unspecified effects

which have effects equivalent to increasing or reducing the amount of mass in the moving structure, during the axial phase. The current factor f_c accounts for the fraction of current effectively flowing in the moving structure (due to all effects such as current shedding at or near the back-wall, and current sheet inclination). This defines the fraction of current effectively driving the structure, during the axial phase.

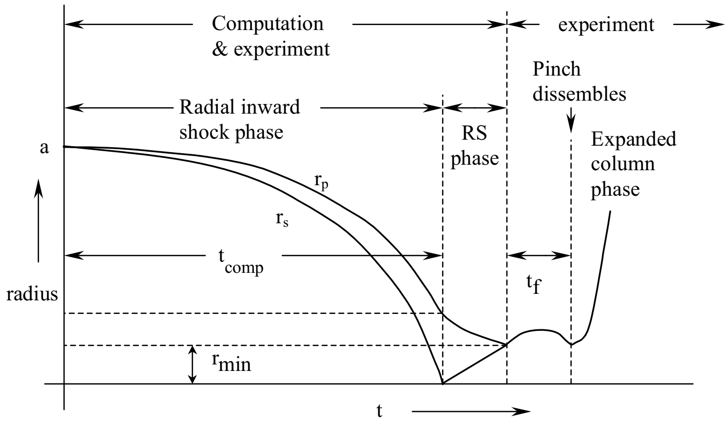

Figure 4. Schematic of radius versus time trajectories to illustrate the radial inward shock phase when r_s moves radially inwards, the reflected shock (RS) phase when the reflected shock moves radially outwards, until it hits the incoming piston r_p leading to the start of the pinch phase (t_f) and finally the expanded column phase.

b. Radial Inward Shock Phase (see Figure 3 right part, also Figure 4): Described by 4 coupled equations using an elongating slug model. The first equation computes the radial inward shock speed from the driving magnetic pressure. The second equation computes the axial elongation speed of the column. The third equation computes the speed of the current sheath, (magnetic piston), allowing the current sheath to separate from the shock front by applying an adiabatic approximation [21]. The fourth is the circuit equation. Thermodynamic effects due to ionization and excitation are incorporated into these equations, these effects being particularly important for gases other than hydrogen and deuterium. Temperature and number densities are computed during this phase using shock-jump equations. A communication delay between shock front and current sheath due to the finite small disturbance speed [14,16,21] is crucially implemented in this phase. The model parameters, radial phase mass swept-up and current factors f_{mr} and f_{cr} are incorporated in all three radial phases. The mass swept-up factor f_{mr} accounts for all mechanisms which have effects equivalent to increasing or reducing the amount of mass in the moving slug, during the radial phase. The current factor f_{cr} accounts for the fraction of current effectively flowing in the moving piston forming the back of the slug (due to all effects). This defines the fraction of current effectively driving the radial slug.

c. Radial Reflected Shock (RS) Phase (See Figure 4): When the shock front hits the axis, because the focus plasma is collisional, a reflected shock develops which moves radially outwards, whilst the radial current sheath piston continues to move inwards. Four coupled equations are also used to describe this phase, these being for the reflected shock moving radially outwards, the piston moving radially inwards, the elongation of the annular column and the circuit. The same model parameters f_{mr} and f_{cr} are used as in the previous radial phase. The plasma temperature behind the reflected shock undergoes a jump by a factor close to 2. Number densities are also computed using the reflected shock jump equations.

d. Slow Compression (Quiescent) or Pinch Phase (See Figure 4): When the out-going reflected shock hits the inward moving piston, the compression enters a radiative phase in which for gases such as neon, radiation emission may actually enhance the compression where we have included energy loss/gain terms from Joule heating and radiation losses into the piston equation of motion. Three coupled equations describe this phase; these being the piston radial motion equation, the pinch column elongation equation and the circuit equation, incorporating the same model parameters as in the previous two phases. The duration of this slow compression phase is set as the time of transit of small disturbances across the pinched plasma column. The computation of this phase is terminated at the end of this duration.

e. Expanded Column Phase: To simulate the current trace beyond this point we allow the column to suddenly attain the radius of the anode, and use the expanded column inductance for further integration. In this final phase the snow plow model is used, and two coupled equations are used similar to the axial phase above. This phase is not considered important as it occurs after the focus pinch.

We note [51] that in radial phases *b, c* and *d*, axial acceleration and ejection of mass caused by necking curvatures of the pinching current sheath result in time-dependent strongly center-peaked density distributions. Moreover the transition from phase *d* to phase *e* is observed in laboratory measurements to occur in an extremely short time with plasma/current disruptions resulting in localized regions of high densities and temperatures. These centre-peaking density effects and localized regions are not modeled in the code, which consequently computes only an average uniform density and an average uniform temperature which are considerably lower than measured peak density and temperature. However, because the four model parameters are obtained by fitting the computed total current waveform to the measured total current waveform, the model incorporates the energy and mass balances equivalent, at least in the gross sense, to all the processes which are not even specifically modeled. Hence the computed gross features such as speeds, trajectories and integrated soft x-ray yields have been extensively tested in numerical experiments for several machines and are found to be comparable with measured values.

5. Modeling as reference for diagnostics

5.1. Fitting the computed to the measured current waveforms

The Lee model code is configured [14,16,28,29, 35-49] to work as any plasma focus by inputting:
Bank parameters, L_0, C_0 and stray circuit resistance r_0;
Tube parameters b, a and z_0 and
Operational parameters V_0 and P_0 and the fill gas.
The computed total current waveform is fitted to the measured waveform by varying model parameters f_m, f_c, f_{mr} and f_{cr} one by one, until the computed waveform agrees with the measured waveform.
First, the axial model factors f_m, f_c are adjusted (fitted) until the features (1) computed rising slope of the total current trace and (2) the rounding off of the peak current as well as (3) the peak current itself are in reasonable (typically very good) fit with the measured total current trace (see Fig 5, measured trace fitted with computed trace).
Then we proceed to adjust (fit) the radial phase model factors f_{mr} and f_{cr} until features (4) the computed slope and (5) the depth of the dip agree with the measured. Note that the fitting of the computed trace with the measured current trace is done up to the end of the radial phase which is typically at the bottom of the current dip. Fitting of the computed and measured current traces

beyond this point is not done. If there is significant divergence of the computed with the measured trace beyond the end of the radial phase, this divergence is not considered important.
In this case, after fitting the 5 features (1) to (5) above, the following fitted model parameters are obtained: f_m=0.1, f_c=0.7, f_{mr}=0.12, f_{cr}=0.68.

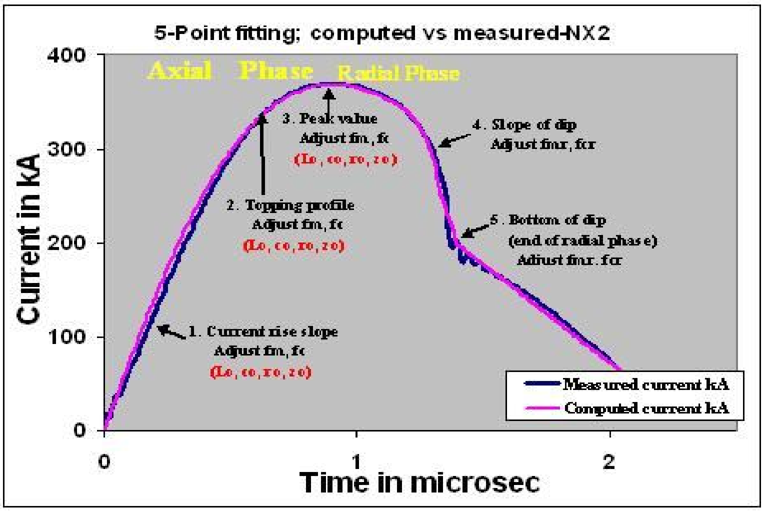

Figure 5. The 5-point fitting of computed current trace to the measured (or the reference) current trace. Point 1 is the current rise slope. Point 2 is the topping profile. Point 3 is the peak value of the current. Point 4 is the slope of the current dip. Point 5 is the bottom of the current dip. Fitting is done up to point 5 only. Further agreement or divergence of the computed trace with/from the measured trace is only incidental and not considered to be important.

5.2. Philosophy for current fitting

From experience it is known that the current trace of the focus is one of the best indicators of gross performance. The axial and radial phase dynamics and the crucial energy transfer into the focus pinch are among the important information that is quickly apparent from the current trace [14,16].
The exact time profile of the total current trace is governed by the bank parameters, by the focus tube geometry and the operational parameters. It also depends on the fraction of mass swept-up and the fraction of sheath current and the variation of these fractions through the axial and radial phases. These parameters determine the axial and radial dynamics, specifically the axial and radial speeds which in turn affect the profile and magnitudes of the discharge current. There are many underlying mechanisms in the axial phase such as shock front and current sheet structure, porosity and inclination, boundary layer effects and current shunting and fragmenting which are not simply modeled; likewise in the radial phase mechanisms such as current sheet curvatures and necking leading to axial acceleration and ejection of mass, and plasma/current disruptions. These effects may give rise to localized regions of high density and temperatures. The detailed profile of the discharge current is influenced by these effects and during the pinch phase also reflects the Joule heating and radiative yields. At the end of the pinch phase the total current profile also reflects the sudden transition of the current flow from a constricted pinch to a large column flow. Thus the discharge current powers all dynamic, electrodynamic, thermodynamic and radiation processes in the various phases of the plasma focus. Conversely all the dynamic, electrodynamic, thermodynamic and radiation processes in the various phases of the plasma focus affect the discharge current. It is then no exaggeration to say that the discharge current

waveform contains information on all the dynamic, electrodynamic, thermodynamic and radiation processes that occur in the various phases of the plasma focus. This explains the importance attached to matching the computed total current trace to the measured total current trace in the procedure adopted by the Lee model code. Once matched, the fitted model parameters assure that the computation proceeds with all physical mechanisms accounted for, at least in the gross energy and mass balance sense.

5.3. Diagnostics-Time histories of dynamics, energies and plasma properties computed from the measured total current waveform by the code

During every adjustment of each of the model parameters the code goes through the whole cycle of computation. In the last adjustment, when the computed total current trace is judged to be reasonably well fitted in all 5 waveform features, computed time histories are presented, in Fig 6a-6o as an example, as follows: for the NX2 operated at 11 kV, 2.6 Torr neon [14,16,31].

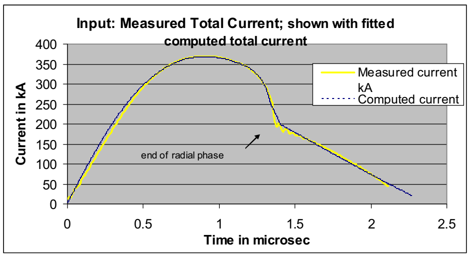

Figure 6a. Fitted computed I_{total}

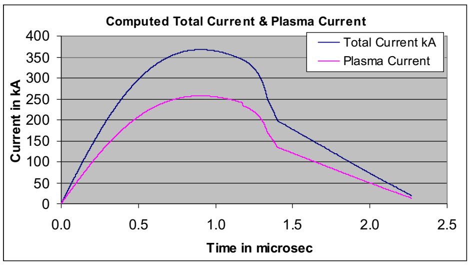

Figure 6b. Computed I_{total} & I_{plasma}

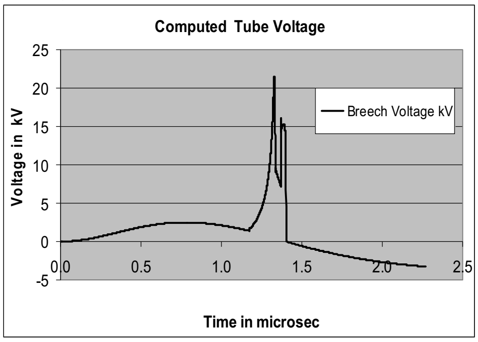

Figure 6c. Tube voltage

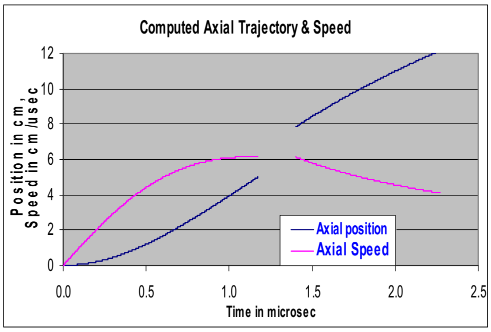

Figure 6d. Axial trajectory and speed

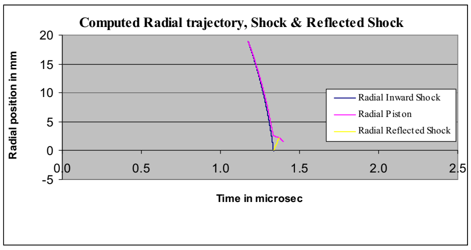

Figure 6e. Radial trajectories

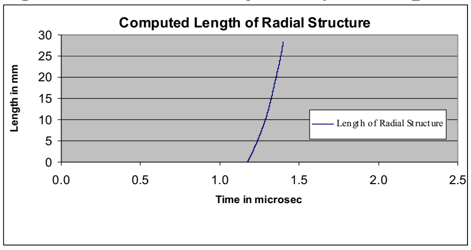

Figure 6f. Length of elongating structure

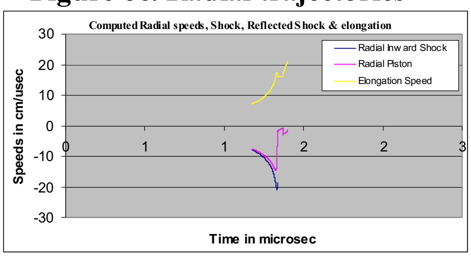

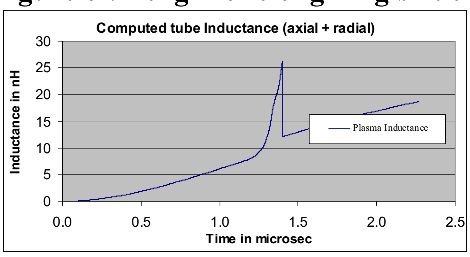

Figure 6g. Speeds in radial phases

Figure 6h. Tube inductance-axial & radial phases

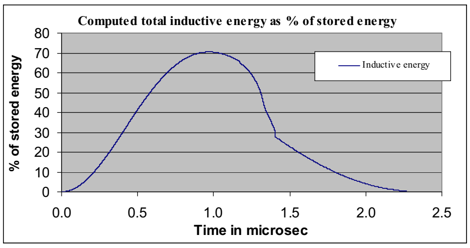

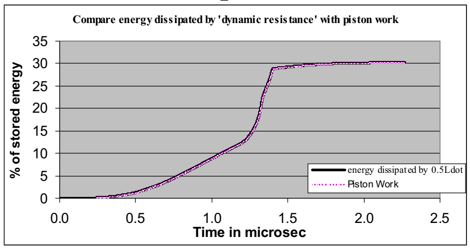

Figure 6i. Total inductive energy

Figure 6j. Piston work and DR energy; both traces overlap

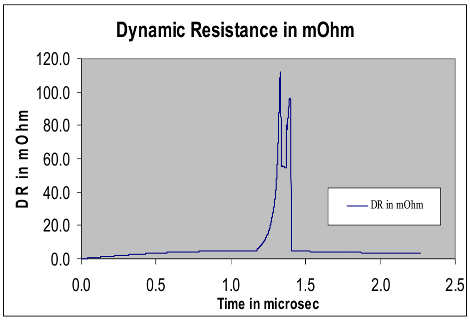

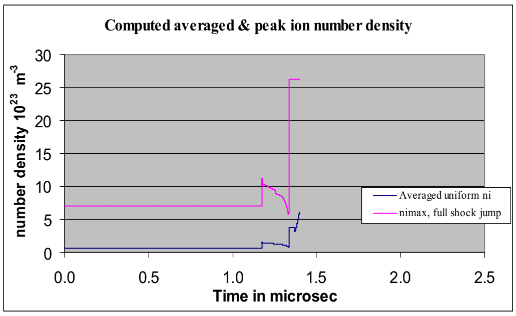

Figure 6k. DR axial and radial phases

Figure 6l. Peak & averaged uniform n_i

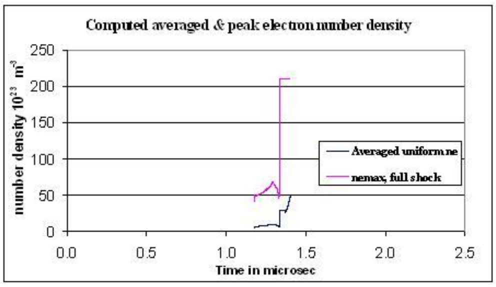

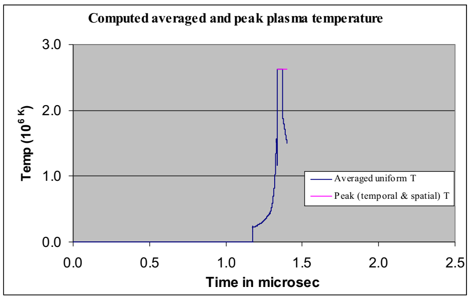

Figure 6m. Peak & averaged uniform n_e

Figure 6n. Peak and averaged uniform T

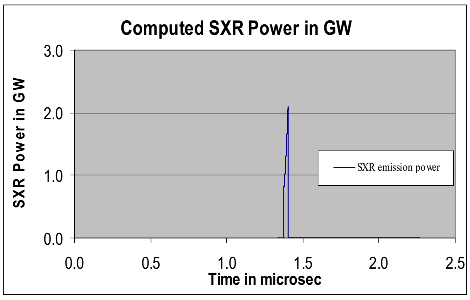

Figure 6o. Neon Soft x-ray power

5.4. Comments on computed quantities

The computed total current trace typically agrees very well with the measured because of the fitting. The end of the radial phase is indicated in Fig. 6a. Plasma currents are rarely measured. We had done a comparison of the computed plasma current with measured plasma current for the Stuttgart PF78 which shows good agreement of our computed to the measured plasma current [36]. The computed plasma current in this case of the NX2 is shown in Fig 6b. The computed tube voltage is difficult to compare with measured tube voltages in terms of peak values, typically because of poor response time of voltage dividers. However the computed waveform shape in Fig 6c. is general as expected. The computed axial trajectory and speed, agree with experimental obtained time histories. Moreover, the behaviour with pressure, running the code again at different pressures, agrees well with experimental results. The radial trajectories and speeds are difficult to measure. The computed trajectories Fig 6e agree with the scant experimental data available. The length of the radial structure is shown in Fig 6f. Computed speeds radial shock front and piston speeds and speed of the elongation of the structure are shown in Fig 6g. The computed inductance (Fig 6h) shows a steady increase of inductance in the axial phase, followed by a sharp increase (rising by more than a factor of 2 in a radial phase time interval about 1/10 the duration of the axial phase for the NX2).

The inductive energy ($0.5LI^2$) peaks at 70% of initial stored energy, and then drops to 30% during the radial phase, as the sharp drop of current more than offsets the effect of sharply increased inductance (Fig 6i). In Fig 6j is shown the work done by the magnetic piston, computed using force integrated over distance method. Also shown is the work dissipated by the dynamic resistance, computed using dynamic resistance power integrated over time. We see that the two quantities and profiles agree exactly. This validates the concept of half Ldot as a dynamic resistance, DR (see section 9.2). The piston work deposited in the plasma increases steadily to some 12% at the end of the axial phase and then rises sharply to just below 30% in the radial phase. Dynamic resistance (DR) is shown in Fig 6k. The values of the DR in the axial phase, together with the bank surge impedance, are the quantities that determine I_{peak}. The ion number density has a maximum value derived from shock-jump considerations, and an averaged uniform value derived from overall energy and mass balance considerations. The time profiles of these are shown in the Fig 6l. The electron number density (Fig 6m) has similar profiles to the ion density profile, but is modified by the effective charge numbers due to ionization stages reached by the ions. Plasma temperature too has a maximum value and an averaged uniform value derived in the same manner; are shown in Fig 6n. Computed neon soft x-ray power profile is shown in Fig 6o. The area of the curve is the soft x-ray yield in Joule. Pinch dimensions and lifetime may be estimated from Figs 6e and 6f. The model also computes the neutron yield, for operation in deuterium, using a phenomenological beam-target mechanism [14,16,35-37]. The model does not compute a time history of the neutron emission, only a yield number Y_n.

Thus as is demonstrated above, the model code when properly fitted is able to realistically model any plasma focus and act as a guide to diagnostics of plasma dynamics, trajectories, energy distribution and gross plasma properties.

6. Insights from Modelling

Moreover, using such simulation, series of experiments have been systematically carried out to look for behaviour patterns of the plasma focus. Insights uncovered by the series of experiments include: (i) pinch current limitation effect as static inductance is reduced; (ii) neutron and SXR scaling laws; (iii) a global scaling law for neutrons versus storage energy combining experimental and numerical experimental data; and (iv) insight into the nature and a fundamental cause of neutron saturation. These are significant achievements accomplished within a period of twenty months of intensive numerical experimentation.

6.1. Insight 1-Pinch Current Limitation Effect as Static Inductance is Reduced Towards Zero

In a recent paper [13] there was expectation that the large MJ plasma focus PF1000 in Warsaw could increase its discharge current, and its pinch current, and consequently neutron yield by a

reduction of its external or static inductance L_0. To investigate this point, experiments were carried out using the Lee Model code. Unexpectedly, the results indicated that whilst I_{peak} indeed progressively increased with reduction in L_0, no improvement may be achieved due to a pinch current limitation effect [37,38]. Given a fixed C_0 powering a plasma focus, there exists an optimum L_0 for maximum I_{pinch}. Reducing L_0 further will increase neither I_{pinch} nor Y_n. The numerical experiments leading to this unexpected result is described below.
A measured current trace of the PF1000 with C_0 = 1332 F, operated at 27 kV, 3.5 torr deuterium, has been published [13], with cathode/anode radii b = 16 cm, a = 11.55 cm and anode length z_0 = 60 cm. In the numerical experiments we fitted external (or static) inductance L_0= 33.5 nH and stray resistance r_0 = 6.1 mΩ (damping factor $RESF= r_0/(L_0/C_0)^{0.5}$ = 1.22). The fitted model parameters are: f_m = 0.13, f_c = 0.7, f_{mr} = 0.35 and f_{cr}= 0.65. The computed current trace [14,35-39] agrees very well with the measured trace through all the phases, axial and radial, right down to the bottom of the current dip indicating the end of the pinch phase as shown in Fig.7.

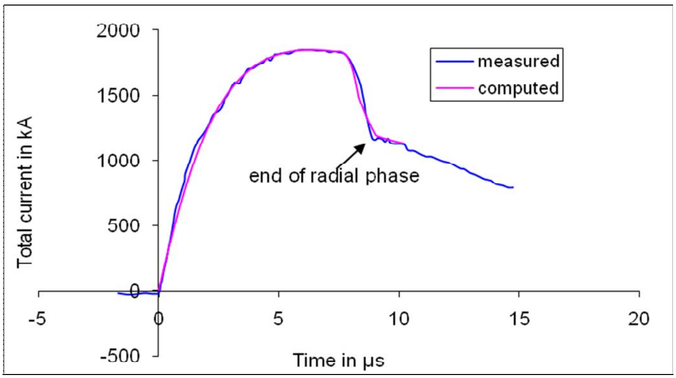

Figure 7. Fitting computed current to measured current traces to obtain fitted parameters f_m = 0.13, f_c= 0.7, f_{mr} = 0.35 and f_{cr}= 0.65. The measured current trace was for the PF1000 at 27 kV, storage capacity of 1332 µF and fitted static inductance of 33.5 µH.

We carried out numerical experiments for PF1000 using the machine and model parameters determined from Figure 7. Operating the PF1000 at 35 kV and 3.5 Torr, we varied the anode radius a with corresponding adjustment to b to maintain a constant c=b/a=1.39 and in order to keep the peak axial speed at 10 cm/µs. The anode length z_0 was also adjusted to maximize I_{pinch} as L_0 was decreased from 100 nH progressively to 5 nH.
As expected, I_{peak} increased progressively from 1.66 to 4.4 MA. As L_0 was reduced from 100 to 35 nH, I_{pinch} also increased, from 0.96 to 1.05 MA. However, then unexpectedly, on further reduction from 35 to 5 nH, I_{pinch} stopped increasing, instead decreasing slightly to 1.03 MA at 20 nH, to 1.0 MA at 10 nH, and to 0.97 MA at 5 nH. Y_n also had a maximum value of 3.2x10^{11} at 35 nH.

6.2. explaining the effect

To explain this unexpected result, we examine the energy distribution in the system at the end of the axial phase (see Fig 7) just before the current drops from peak value I_{peak} and then again near the bottom of the almost linear drop to the pinch phase indicated by the arrow pointing to ‘end of radial phase’. The energy equation describing this current drop is written as follows:

$$0.5I_{peak}^2(L_0 + L_a f_c^{\,2})= 0.5I_{pinch}^2 (L_0/f_c^2 + L_a + L_p) + \delta_{cap}+ \delta_{plasma}, \quad (1)$$

where L_a is the inductance of the tube at full axial length z_0, δ_{plasma} is the energy imparted to the plasma as the current sheet moves to the pinch position and is the integral of $0.5(dL/dt)I^2$. We approximate this as $0.5L_pI_{pinch}^2$ which is an underestimate for this case. δ_{cap} is the energy flow into or out of the capacitor during this period of current drop. If the duration of the radial phase is short compared to the capacitor time constant, the capacitor is effectively decoupled and δ_{cap} may be put as zero. From this consideration we obtain

$$I_{pinch}^2 = I_{\mathrm{peak}}^2(L_0 + 0.5L_a)/(2L_0 + L_a + 2L_p), \tag{2}$$

where we have taken f_c=0.7 and approximated $f_c^{\ 2}$ as 0.5.
Generally, as L_0 is reduced, I_{peak} increases; a is necessarily increased leading [9] to a longer pinch length z_p, hence a bigger L_p. Lowering L_o also results in a shorter rise time, hence a necessary decrease in z_0, reducing L_a. Thus, from Eq. (2), lowering L_0 decreases the fraction I_{pinch}/I_{peak}. Secondly, this situation is compounded by another mechanism. As L_0 is reduced, the L-C interaction time of the capacitor bank reduces while the duration of the current drop increases (see Fig ~~6~~ 8, discussed in the next section) due to an increasing a. This means that as L_0 is reduced, the capacitor bank is more and more coupled to the inductive energy transfer processes with the accompanying induced large voltages that arise from the radial compression. Looking again at the derivation of Eq. (2) from Eq. (1) a nonzero δ_{cap}, in this case, of positive value, will act to decrease I_{pinch} further. The lower the L_0 the more pronounced is this effect.
Summarizing this discussion, the pinch current limitation is not a simple effect, but is a combination of the two complex effects described above, namely, the interplay of the various inductances involved in the plasma focus processes abetted by the increasing coupling of C_o to the inductive energetic processes, as L_0 is reduced.

6.3. Optimum L_0 for maximum pinch current and neutron yield

From the pinch current limitation effect, it is clear that given a fixed C_0 powering a plasma focus, there exists an optimum L_0 for maximum I_{pinch}. Reducing L_0 further will increase neither I_{pinch} nor Y_n. The results of the numerical experiments carried out are presented in Figure 8 and Table 4.
With large L_0 = 100 nH it is seen (Figure 8) that the rising current profile is flattened from what its waveform would be if unloaded; and peaks at around 12 s (before its unloaded rise time, not shown, of 18 s) as the current sheet goes into the radial phase. The current drop, less than 25% of peak value, is sharp compared with the current rise profile. At L_0 = 30 nH the rising current profile is less flattened, reaching a flat top at around 5 s, staying practically flat for some 2 s before the radial phase current drop to 50% of its peak value in a time which is still short compared with the rise time. With L_0 of 5 nH, the rise time is now very short, there is hardly any flat top; as soon as the peak is reached, the current waveform droops significantly. There is a small kink on the current waveform of both the L_0 = 5 nH, z_0 = 20 cm and the L_0= 5 nH, z_0 = 40 cm. This kink corresponds to the start of the radial phase which, because of the large anode radius, starts with a relatively low radial speed, causing a momentary reduction in dynamic loading. Looking at the three types of traces it is seen that for L_0 = 100 nH to 30 nH, there is a wide range of z_0 that may be chosen so that the radial phase may start at peak or near peak current, although the longer values of z_0 tend to give better energy transfers into the radial phase.

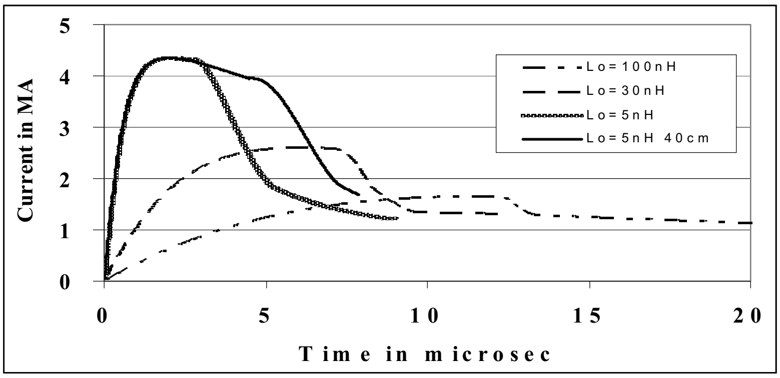

Figure 8. PF1000 current waveforms computed at 35kV, 3.5 Torr D_2 for a range of L_0 showing the changes in waveforms as L_0 varies.

The optimized situation for each value of L_0 is shown in Table 4. The table shows that as L_0 is reduced, I_{peak} rises with each reduction in L_0 with no sign of any limitation. However, I_{pinch} reaches a broad maximum of 1.05MA around 40–30 nH. Neutron yield Y_n also shows a similar broad maximum peaking at 3.2×10^{11} neutrons. Figure 9 shows a graphical representation of this I_{pinch} limitation effect. The curve going up to 4MA at low L_0 is the I_{peak} curve. Thus I_{peak} shows no sign of limitation as L_0 is progressively reduced. However I_{pinch} reaches a broad maximum. From Fig 9 there is a stark and important message. One must distinguish clearly between I_{peak} and I_{pinch}. In general one cannot take I_{peak} to be representative of I_{pinch}.

Table 4. Currents and ratio of currents as L_o is reduced-PF1000 at 35kV, 3.5 Torr Deuterium

L_0(nH)	b(cm)	a(cm)	z_0(cm)	I_{peak}(MA)	I_{pinch}(M)	Y_n(10^{11})	I_{pinch}/I_{peak}
100	15.0	10.8	80	1.66	0.96	2.44	0.58
80	16.0	11.6	80	1.81	1.00	2.71	0.55
60	18.0	13.0	70	2.02	1.03	3.01	0.51
40	21.5	15.5	55	2.36	1.05	3.20	0.44
35	22.5	16.3	53	2.47	1.05	3.20	0.43
30	23.8	17.2	50	2.61	1.05	3.10	0.40
20	28.0	21.1	32	3.13	1.03	3.00	0.33
10	33.0	23.8	28	3.65	1.00	2.45	0.27
5	40.0	28.8	20	4.37	0.97	2.00	0.22

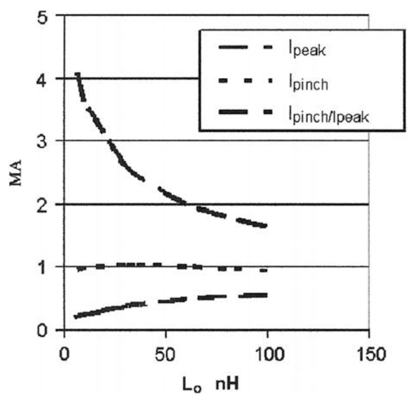

Figure 9. Currents and current ratio (computed) as L_0 is reduced PF1000, 35 kV, 3.5 torr D_2

We carried out several sets of experiments on the PF1000 for varying L_0, each set with a different damping factor. In every case, an optimum inductance was found around 30–60 nH with I_{pinch} decreasing as L_0 was reduced below the optimum value. The results showed that for PF1000, reducing L_0 from its present 20–30 nH will increase neither the observed I_{pinch} nor the neutron yield, because of the pinch limitation effect. Indeed, the I_{pinch} decreases very slightly on further reduction to very small values. We would add that we have used a set of model parameters which in our experience is the most reasonable to be used in these numerical experiments. Variations of the model parameters could occur but we are confident that these variations are not likely to occur with such a pattern as to negate the pinch current limitation effect. Nevertheless these variations should be actively monitored and any patterns in the variations should be investigated.

7. Insight 2-Scaling Laws for Neutron

7.1. Computation of Neutron yield-describing the beam-target mechanism

The neutron yield is computed using a phenomenological beam-target neutron generating mechanism described recently by Gribkov et al [13] and adapted to yield the following equation. A beam of fast deuteron ions is produced by diode action in a thin layer close to the anode, with plasma disruptions generating the necessary high voltages. The beam interacts with the hot dense plasma of the focus pinch column to produce the fusion neutrons. The beam-target yield is derived [14,16, 35-39] as:

$$Y_{b\text{-}t}= C_n\, n_i\, I_{pinch}{}^2 z_p{}^2 (\ln (b/r_p))\sigma /U^{0.5} \tag{3}$$

where n_i is the ion density, b is the cathode radius, r_p is the radius of the plasma pinch with length z_p, σ the cross-section of the D-D fusion reaction, n- branch [52] and U, the beam energy. C_n is treated as a calibration constant combining various constants in the derivation process.

The D-D cross-section is sensitive to the beam energy in the range 15-150 kV; so it is necessary to use the appropriate range of beam energy to compute σ. The code computes induced voltages (due to current motion inductive effects) V_{max} of the order of only 15-50 kV. However it is known, from experiments that the ion energy responsible for the beam-target neutrons is in the range 50-150 keV [5,13], and for smaller lower-voltage machines the relevant energy could be lower at 30-60 keV [27]. Thus in line with experimental observations the D-D cross section σ is reasonably obtained by using $U = 3V_{max}$. This fit was tested by using U equal to various multiples of V_{max}. A reasonably good fit of the computed neutron yields to the measured published neutron yields at energy levels from sub-kJ to near MJ was obtained when the multiple of 3 was used; with poor agreement for most of the data points when for example a multiple of 1 or 2 or 4 or 5 was used. The model uses a value of C_n=2.7x10^7 obtained by calibrating the yield [14,16,35], at an experimental point of 0.5 MA.

The thermonuclear component is also computed in every case and it is found that this component is negligible when compared with the beam-target component. It might be argued that an adjustment to the thermonuclear component could also be attempted in a similar way to the usage of the multiple to V_{max}. However, the usage of the multiple to V_{max} has some experimental basis due to ion energy measurements. Moreover the value of V_{max} in each numerical experiment is calculated from the slug model leading to the slow compression phase, whilst it is known experimentally that after the slow compression phase, instability effects set in which will increase the electric fields operating within the pinch. These are the basic arguments supporting the view that the operational beam energy has a value above V_{max}. For the thermonuclear component a feasible model to adjust the yield upwards has yet to be suggested.

7.2. Scaling laws for neutrons from numerical experiments over a range of energies from 10kJ to 25 MJ

We apply the Lee model code to the MJ machine PF1000 over a range of C_0 to study the neutrons emitted by PF1000-like bank energies from 10kJ to 25 MJ.
As shown earlier the PF1000 current trace has been used to fit the model parameters, with very good fitting achieved between the computed and measured current traces (Fig 7). Once the model parameters have been fitted to a machine for a given gas, these model parameters may be used with some degree of confidence when operating parameters such as the voltage are varied [35,39]. With no measured current waveforms available for the higher megajoule numerical experiments, it is reasonable to keep the model parameters that we have got from the PF1000 fitting.
The optimum pressure for this series of numerical experiments is 10 torr and the ratio $c=b/a$ is retained at 1.39. For each C_0, anode length z_0 is varied to find the optimum. For each z_0, anode radius a_0 is varied so that the end axial speed is 10 cm/μs. The numerical experiments were carried out for C_0 ranging from 14 μF to 39960 μF corresponding to energies from 8.5 kJ to 24.5MJ [10].
For this series of experiments we find that the Y_n scaling changes from $Y_n \sim E_0^{2.0}$ at tens of kJ to $Y_n \sim E_0^{0.84}$ at the highest energies (up to 25MJ) investigated in this series. This is shown in Fig 10.

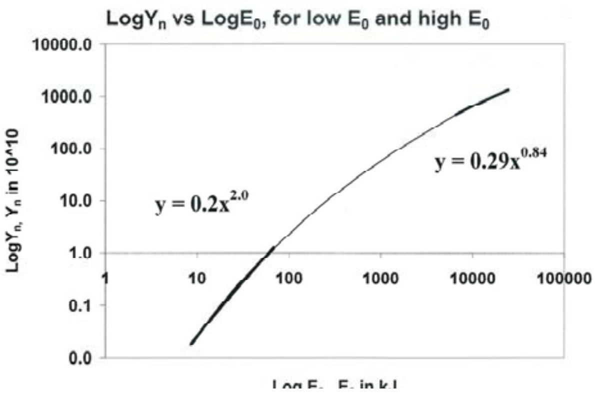

Figure 10. Y_n plotted as a function of E_0 in log-log scale, showing Y_n scaling changes from $Y_n \sim E_0^{2.0}$ at tens of kJ to $Y_n \sim E_0^{0.84}$ at the highest energies (up to 25MJ). This scaling deterioration is discussed in Section 9.2

The scaling of Y_n with I_{peak} and I_{pinch} over the whole range of energies investigated up to 25 MJ (shown in Figure 11) are as follows:

$Y_n = 3.2\text{x}10^{11} I_{pinch}^{4.5}$ and
$Y_n = 1.8\text{x}10^{10} I_{peak}^{3.8}$

where I_{peak} ranges from 0.3 MA to 5.7 MA and I_{pinch} ranges from 0.2 MA to 2.4 MA.

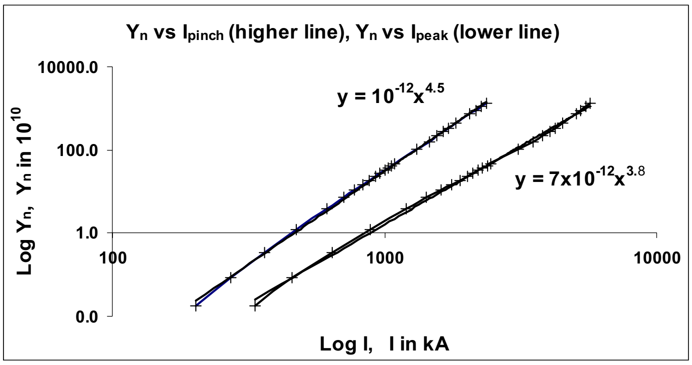

Figure 11. Log(Y_n) scaling with Log(I_{peak}) and Log(I_{pinch}), for the range of energies investigated, up to 25 MJ

This compares to an earlier study carried out on several machines with published current traces and Y_n yield measurements, operating conditions and machine parameters including the Chilean PF400J, the UNU/ICTP PFF, the NX2 and Poseidon providing a slightly higher scaling laws:

$Y_n \sim I_{pinch}^{4.7}$ and
$Y_n \sim I_{peak}^{3.9}$

The slightly higher value of the scaling is because those machines fitted are of mixed '*c*' mixed bank parameters, mixed model parameters and currents generally below 1MA and voltages generally below the 35 kV [35].

7.3. Summary of neutron scaling laws from numerical experiments:

Over wide ranges of energy, optimizing pressure, anode length and radius, the scaling laws for Y_n [10,35,41,43] obtained through numerical experiments are listed here:

Y_n=3.2x10$^{11}I_{pinch}^{4.5}$

Y_n=1.8x10$^{10}I_{peak}^{3.8}$ $\quad$ I_{peak} (0.3 to 5.7), I_{pinch} (0.2 to 2.4) in MA.

$Y_n \sim E_0^{2.0}$ at tens of kJ to

$Y_n \sim E_0^{0.84}$ at MJ level (up to 25MJ)

These laws provide useful references and facilitate the understanding of present plasma focus machines. More importantly, these scaling laws are also useful for design considerations of new plasma focus machines particularly if they are intended to operate as optimized neutron sources.

8. Insight 3-Scaling Laws for Soft X-ray Yield

8.1. Computation of Neon SXR yield

We note that the transition from Phase 4 to Phase 5 is observed in laboratory measurements to occur in an extremely short time with plasma/current disruptions resulting in localized regions of high densities and temperatures. These localized regions are not modelled in the code, which consequently computes only an average uniform density, and an average uniform temperature which are considerably lower than measured peak density and temperature. However, because the 4 model parameters are obtained by fitting the computed total current waveform to the measured total current waveform, the model incorporates the energy and mass balances equivalent, at least in the gross sense, to all the processes which are not even specifically modelled. Hence the computed gross features such as speeds and trajectories and integrated soft x-ray yields have been extensively tested in numerical experiments for several machines and are found to be comparable with measured values.

In the code [14,16,44], neon line radiation Q_L is calculated as follows:

$$\frac{dQ_L}{dt} = -4.6x10^{-31} n_i^{\,2} Z Z_n^4 \left(\pi r_p^2\right) z_{\mathrm{f}} / T \tag{4}$$

where for the temperatures of our interest we take the SXR yield $Y_{sxr} = Q_L$. Z_n is atomic number. Hence the SXR energy generated within the plasma pinch depends on the properties: number density n_i, effective charge number Z, pinch radius r_p, pinch length z_f and temperature T. It also depends on the pinch duration since in our code Q_L is obtained by integrating over the pinch duration.

This generated energy is then reduced by the plasma self-absorption which depends primarily on density and temperature; the reduced quantity of energy is then emitted as the SXR yield. These effects are included in the modelling by computing volumetric plasma self-absorption factor A derived from the photonic excitation number M which is a function of Z_n, n_i, Z and T. However, in our range of operation, the numerical experiments show that the self absorption is not significant. It was first pointed out by Liu Mahe [22,25] that a temperature around 300 eV is optimum for SXR production. Shan Bing's subsequent work [23] and our experience through numerical experiments suggest that around $2x10^6$ K (below 200 eV) or even a little lower could be better. Hence unlike the case of neutron scaling, for SXR scaling there is an optimum small range of temperatures (T windows) to operate.

8.2. Scaling laws for neon SXR over a range of energies from 0.2 kJ to 1 MJ

We next use the Lee model code to carry out a series of numerical experiments over the energy range 0.2 kJ to 1 MJ [44]. In this case we apply it to a proposed modern fast plasma focus machine with optimised values for c the ratio of the outer to inner electrode radius and L_0 obtained from our numerical experiments.

The following parameters are kept constant : (i) the ratio $c=b/a$ (kept at 1.5, which is practically optimum according to our preliminary numerical trials; (ii) the operating voltage V_0 (kept at 20 kV); (iii) static inductance L_0 (kept at 30 nH, which is already low enough to reach the I_{pinch} limitation regime [37,38] over most of the range of E_0 we are covering) and; (iv) the ratio of stray resistance to surge impedance *RESF* (kept at 0.1, representing a higher performance modern capacitor bank). The model parameters [46] f_m, f_c, f_{mr}, f_{cr} are also kept at fixed values 0.06, 0.7, 0.16 and 0.7. We choose the model parameters so they represent the average values from the range of machines that we have studied. A typical example of a current trace for these parameters is shown in Fig 12.

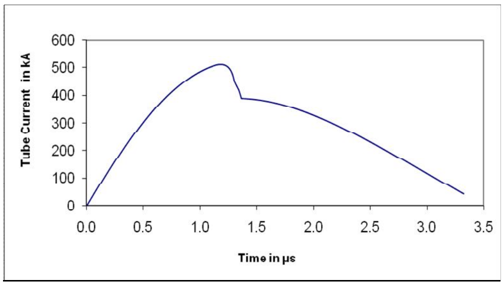

Figure 12. Computed total curent versus time for L_0= 30 nH and V_0 = 20 kV, C_0 = 30 μF, *RESF* = 0.1, *c* = 1.5 and model parameters f_m, f_c, f_{mr}, f_{cr} are fixed at 0.06, 0.7, 0.16 and 0.7 for optimised *a* = 2.285cm and z_0 = 5.2 cm.

The storage energy E_0 is varied by changing the capacitance C_0. Parameters that are varied are operating pressure P_0, anode length z_0 and anode radius *a*. Parametric variation at each E_0 follows the order; P_0, z_0 and *a* until all realistic combinations of P_0, z_0 and *a* are investigated. At each E_0, the optimum combination of P_0, z_0 and *a* is found that produces the biggest Y_{sxr}. In other words at each E_0, a P_0 is fixed, a z_0 is chosen and *a* is varied until the largest Y_{sxr} is found. Then keeping the same values of E_0 and P_0, another z_0 is chosen and *a* is varied until the largest Y_{sxr} is found. This procedure is repeated until for that E_0 and P_0, the optimum combination of z_0 and *a* is found. Then keeping the same value of E_0, another P_0 is selected. The procedure for parametric variation of z_0 and *a* as described above is then carried out for this E_0 and new P_0 until the optimum combination of z_0 and *a* is found. This procedure is repeated until for a fixed value of E_0, the optimum combination of P_0, z_0 and *a* is found.
The procedure is then repeated with a new value of E_0. In this manner after systematically carrying out some 2000 runs, the optimized runs for various energies are tabulated in Table 5. We plot Y_{sxr} against E_0 as shown in Fig 13.

Table 5. Optimised configuration found for each E_0. Optimisation carried out with RESF = 0.1, c = 1.5, L_0 = 30 nH and V_0 = 20 kV and model parameters f_m, f_c, f_{mr}, f_{cr} are fixed at 0.06, 0.7, 0.16 and 0.7 respectively. The v_a, v_s and v_p are the peak axial, radial shock and radial piston speeds respectively.

E_0 (kJ)	C_0 (μF)	*a* (cm)	z_0 (cm)	P_0 (Torr)	I_{peak} (kA)	I_{pinch} (kA)	v_a (cm/μs)	v_s (cm/μs)	v_p (cm/μs)	Y_{sxr} (J)
0.2	1	0.58	0.5	4.0	100	68	5.6	22.5	14.9	0.44
1	5	1.18	1.5	4.0	224	143	6.6	23.3	15.1	7.5
2	10	1.52	2.1	4.0	300	186	6.8	23.6	15.2	20
6	30	2.29	5.2	4.2	512	294	8.1	24.5	15.6	98
10	50	2.79	7.5	4.0	642	356	8.7	24.6	15.7	190
20	100	3.50	13	4.0	861	456	9.6	24.6	16.0	470
40	200	4.55	20	3.5	1109	565	10.3	24.7	16.2	1000
100	500	6.21	42	3.0	1477	727	11.2	24.8	16.4	2700
200	1000	7.42	63	3.0	1778	876	11.4	24.8	16.5	5300
400	2000	8.70	98	3.0	2079	1036	11.4	24.9	16.5	9400
500	2500	9.10	105	2.9	2157	1086	11.5	25.1	16.7	11000
1000	5000	10.2	160	3.0	2428	1261	11.4	25.2	16.7	18000

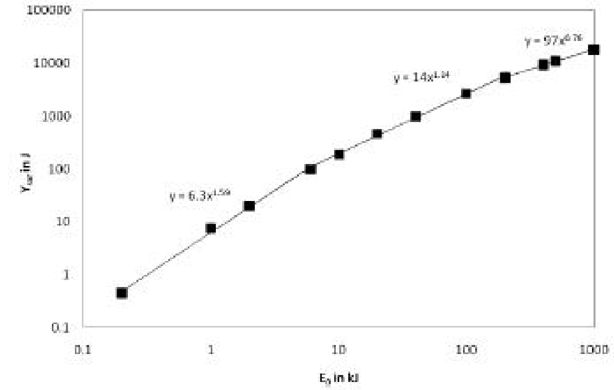

Figure 13. Ysxr vs E_0. The parameters kept constants are: RESF=0.1, c=1.5, L_0=30nH and V_0=20 kV and model parameters f_m, f_c, f_{mr}, f_{cr} at 0.06, 0.7, 0.16 and 0.7 respectively. The scaling deterioration observed in this Figure is similar to that for neutron yield and is discussed in section 9.2.

We then plot Y_{sxr} against I_{peak} and I_{pinch} and obtain SXR yield scales as

$Y_{sxr} \sim I_{pinch}^{3.6}$ and
$Y_{sxr} \sim I_{peak}^{3.2}$.

The I_{pinch} scaling has less scatter than the I_{peak} scaling. We next subject the scaling to further test when the fixed parameters *RESF*, *c*, L_0 and V_0 and model parameters f_m, f_c, f_{mr}, f_{cr} are varied. We add in the results of some numerical experiments using the parameters of several existing plasma focus devices including the UNU/ICTP PFF (*RESF* = 0.2, *c* = 3.4, L_0 = 110 nH and V_0 = 14 kV with fitted model parameters f_m = 0.05, f_c = 0.7, f_{mr} = 0.2, f_{cr} = 0.8) [14,16,22,23,25,32,48], the NX2 (*RESF* = 0.1, *c* = 2.2, L_0 = 20 nH and V_0 = 11 kV with fitted model parameters f_m = 0.10, f_c = 0.7, f_{mr} = 0.12, f_{cr} = 0.68) [14,16,22,23,31,46], and PF1000 (*RESF* = 0.1, *c* = 1.39, L_0 = 33 nH and V_0 = 27 kV with fitted model parameters f_m = 0.1, f_c = 0.7, f_{mr} = 0.15, f_{cr} = 0.7) [14,16,36,37]. These new data points (white data points in Fig. 14) contain wide ranges of *c*, V_0, L_0 and model parameters. The resulting Y_{sxr} versus I_{pinch} log-log curve remains a straight line, with the scaling index 3.6 unchanged and with no more scatter than before. However the resulting Y_{sxr} versus I_{peak} curve now exhibits considerably larger scatter and the scaling index has changed slightly (note the change is not shown/obvious here).

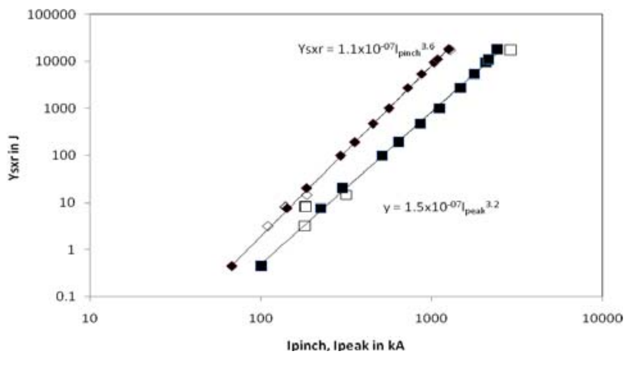

Figure 14. Y_{sxr} is plotted as a function of I_{pinch} and I_{peak}. The parameters kept constant for the black data points are: *RESF* = 0.1, *c* = 1.5, L_0 = 30nH and V_0 = 20 kV and model parameters f_m, f_c, f_{mr}, f_{cr} at 0.06, 0.7, 0.16 and 0.7 respectively. The white data points are for specific machines which have different values for the parameters *c*, L_0 and V_0.

We would like to highlight that the consistent behaviour of I_{pinch} in maintaining the scaling of $Y_{sxr} \sim I_{pinch}^{3.6}$ with less scatter than the $Y_{sxr} \sim I_{peak}^{3.2}$ scaling particularly when mixed-parameters cases are included, strongly supports the conclusion that I_{pinch} scaling is the more universal and robust one. Similarly conclusions on the importance of I_{pinch} in plasma focus performance and scaling laws have been reported [36].

It may also be worthy of note that our comprehensively surveyed numerical experiments for Mather configurations in the range of energies 0.2 kJ to 1 MJ produce an I_{pinch} scaling rule for Y_{sxr} not compatible with Gates' rule [53]. However it is remarkable that our I_{pinch} scaling index of 3.6, obtained through a set of comprehensive numerical experiments over a range of 0.2 kJ to 1 MJ, on Mather-type devices, is within the range of 3.5 to 4 postulated on the basis of sparse experimental data, (basically just two machines one at 5 kJ and the other at 0.9 MJ), by Filippov [54], for Filippov configurations in the range of energies 5 kJ to 1 MJ.

It must be pointed out that the results represent scaling for comparison with baseline plasma focus devices that have been optimized in terms of electrode dimensions. It must also be emphasized that the scaling with I_{pinch} works well even when there are some variations in the actual device from L_0= 30 nH, V_0= 20 kV and c = 1.5.

8.3. Summary of Soft X-ray scaling laws found by numerical experiments:

Over wide ranges of energy, optimizing pressure, anode length and radius, the scaling laws for neon SXR are found by numerical experiments to be:

$Y_{sxr}=8.3\text{x}10^3\text{x}I_{pinch}^{3.6}$

$Y_{sxr}=600\text{x}I_{peak}^{3.2}$; I_{peak} (0.1 to 2.4), I_{pinch} (0.07 to1.3) in MA.

Y_{sxr}~$E_0^{1.6}$ (kJ range) to

Y_{sxr}~$E_0^{0.8}$ (towards MJ).

These laws provide useful references and facilitate the understanding of present plasma focus machines. More importantly, these scaling laws are also useful for design considerations of new plasma focus machines particularly if they are intended to operate as neon SXR sources.

9. Insight 4- Neutron Saturation

Besides being accurately descriptive and related to wide-ranging experimental reality, desirable characteristics of a model include predictive and extrapolative scaling. Moreover a useful model should be accessible, usable and user-friendly and should be capable of providing insights. Insight however cannot be a characteristic of the model in isolation, but is the interactive result of the model with the modeler or model user.

It was observed early in plasma focus research [5,9] that neutron yield $Y_n \sim E_0^2$ where E_0 is the capacitor storage energy. Such scaling gave hopes of possible development as a fusion energy source. Devices were scaled up to higher E_0. It was then observed that the scaling deteriorated, with Y_n not increasing as much as suggested by the E_0^2 scaling. In fact some experiments were interpreted as evidence of a neutron saturation effect [5] as E_0 approached several hundreds of kJ. As recently as 2006 Krauz [55] and November 2007, Scholz [56] have questioned whether the neutron saturation was due to a fundamental cause or to avoidable machine effects such as incorrect formation of plasma current sheath arising from impurities or sheath instabilities. We should note here that the region of discussion (several hundreds of kJ approaching the MJ region) is in contrast to the much higher energy region discussed by Schmidt at which there might be expected to be a decrease in the role of beam target fusion processes[5].

9.1. The global neutron scaling law

Recent extensive numerical experiments [10,11,35,42,51] also showed that whereas at energies up to tens of kJ the $Y_n \sim E_0^2$ scaling held, deterioration of this scaling became apparent above the low hundreds of kJ. This deteriorating trend worsened and tended towards $Y_n \sim E_0^{0.8}$ at tens of MJ. The results of these numerical experiments are summarized in Fig.1 (Section 2 above) with the solid line representing results from numerical experiments. Experimental results from 0.4 kJ to MJ, compiled from several available published sources [4,5,9,13,15,35, 55-58], are also included as squares in the same figure. The combined experimental and numerical experimental results [11,42,51] (see Fig 1 in Section 2 above) appear to have general agreement particularly with regards to the $Y_n \sim E_0^2$ at energies up to 100 kJ, and the deterioration of the scaling from low hundreds of kJ to the 1 MJ level. The global data of Fig. 1 suggests that the apparently observed neutron saturation effect is overall not in significant variance with the deterioration of the scaling shown by the numerical experiments.

9.2. The dynamic resistance

A simple yet compelling analysis of the cause of this neutron saturation has been published [11]. In Fig. 3 (see Section 4 above) on the left side is shown a schematic of the plasma dynamics in the axial phase of the Mather-type plasma focus. In that work the simplest representation was used, in which the current sheet is shown to go from the anode to the cathode perpendicularly. Observation shows that there is actually a canting of the current sheet [18,26,50] and also that only a fraction (typically 0.7) of the total current participates in driving the current sheet. These points are accounted for in the modelling by model parameters f_m and f_c. We now represent the plasma focus circuit in Fig 15.

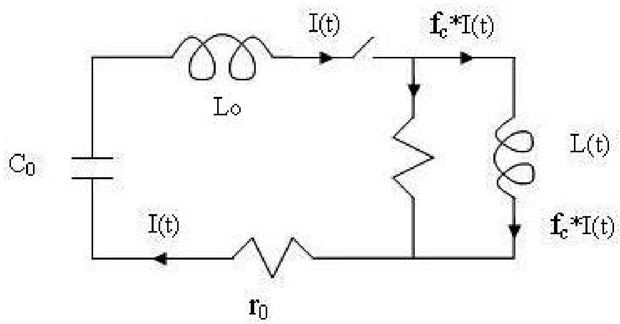

Figure 15. Plasma focus circuit schematic. The capacitor bank with static inductance L_0 and stray resistance r_0 is switched into the plasma focus tube where a fraction f_c of the circuit current I(t) effectively drives the plasma creating a time-varying inductance L(t) in the focus tube.

We consider only the axial phase. By surveying published results of all Mather-type experiments we find that all deuterium plasma focus devices operate at practically the same speeds [6] and are characterized by a constancy of energy density (per unit mass) over the whole range of devices from the smallest sub-kJ to the largest MJ devices. The time varying tube inductance is

$L=(\mu/2\pi)ln(c)\ z$, where $c=b/a$ and μ is the permeability of free space. The rate of change of inductance is $dL/dt=2x10^{-7}(lnc)\ dz/dt$ in SI units. Typically on switching, as the capacitor discharges, the current rises towards its peak value, the current sheet is accelerated, quickly reaching nearly its peak speed and continues accelerating slightly towards its peak speed at the end of the axial phase. Thus for most of its axial distance the current sheet is travelling at a speed close to the end-axial speed. In deuterium the end-axial speed is observed to be about 10 cm/ μs over the whole range of devices [6]. This fixes the rate of change of inductance dL/dt as $1.4x10^{-2}$H/s for all the devices, if we take the radius ratio $c=b/a=2$. This value of dL/dt changes by at most a factor of 2, taking into account the variation of c from low values of 1.4 (generally for larger machines) to 4 (generally for smaller machines). This typical dL/dt may also be expressed as 14 mΩ.

We need now to inquire into the nature of the change in the inductance $L(t)$.
Consider instantaneous power P delivered to $L(t)$ by a change in $L(t)$

Induced voltage: $$V=d(LI)/dt= I(dL/dt)+L(dI/dt) \tag{5}$$

Hence instantaneous power into $L(t)$: $$P=VI= I^2(dL/dt)+LI(dI/dt) \tag{6}$$

Next, consider instantanteous power associated with the inductive energy $(½LI^2)$:

$$P_L=d(½LI^2)/dt= ½I^2(dL/dt)+LI(dI/dt) \tag{7}$$

We note that P_L of Eq (7) is not the same as P of Eq (6).
The difference= $P- P_L$ = (½) $(dL/dt)I^2$ is not associated with the inductive energy stored in L. We conclude that whenever $L(t)$ changes with time, the instantaneous power delivered to $L(t)$ has a component that is not inductive. Hence this component of power $(½)(dL/dt)I^2$ must be resistive in nature; and the quantity $(½)(dL/dt)$ also denoted as half Ldot is identified as a resistance, due to the motion associated with dL/dt ; which we call the dynamic resistance DR,[10,11,39,42,51]. Note that this is a general result and is independent of the actual processes involved. In the case of the plasma focus axial phase, the motion of the current sheet imparts power to the shock wave structure with consequential shock heating, Joule heating, ionization, radiation etc. The total power imparted at any instant is just the amount $(½)\ (dL/dt)I^2$, with this amount powering all consequential processes. We denote the dynamic resistance of the axial phase as DR_0.
We have thus identified for the axial phase of the plasma focus a typical dynamic resistance of 7 mΩ due to the motion of the current sheet at 10 cm/ μ s. It should be noted here that similar ideas of the role of dL/dt as a resistance were discussed by Bernard et al [5]. In that work the effect of dL/dt was discussed only for the radial phase. In our opinion the more important phase for the purpose of neutron saturation is actually the axial phase for the Mather-type plasma focus.

9.3. The interaction of a constant dynamic resistance with a reducing generator impedance causes deterioration in current scaling

We now resolve the problem into its most basic form as follows. We have a generator (the capacitor charged to 30 kV), with an impedance of $Z_0=(L_0/C_0)^{0.5}$ driving a load with a near constant resistance of 7 mΩ. We also assign a value for stray resistance of $0.1Z_0$. This situation may be shown in Table 6 where L_0 is given a typical value of 30 nH. We also include in the last column the results from a circuit (L-C-R) computation, discharging the capacitor with initial voltage 30 kV into a fixed resistance load of 7mΩ simulating the effect of the DR_0 and a stray resistance of value $0.1Z_0$.

Table 6. Discharge characteristics of equivalent PF circuit, illustrating the 'saturation' of I_{peak} with increase of E_0 to very large values. The last column presents results using circuit (L-C-R) computation, with a fixed resistance load of 7 mΩ, simulating the effect of the DR_0 and a stray resistance of value $0.1Z_0$.

E_0 (kJ)	C_0 (μF)	Z_0 (mΩ)	$\mathbf{DR_0}$ (mΩ)	Z_{total} (mΩ)	$I_{peak}=V_0/Z_{total}$ (kA)	I_{peak},L-C-R (kA)
0.45	1	173	7	197	152	156
4.5	10	55	7	67	447	464
45	100	17	7	26	1156	1234
135	300	10	7	18	1676	1819
450	1000	5.5	7	12.9	2321	2554
1080	2400	3.5	7	10.8	2781	3070
4500	10000	1.7	7	8.8	3407	3722
45000	100000	0.55	7	7.6	4209	4250

Plotting the peak current as a function of E_0 we obtain Fig 16, which shows the tendency of the peak current towards saturation as E_0 reaches large values; the deterioration of the curve becoming apparent at the several hundred kJ level. This is the case for $I_{peak}=V_0/Z_{total}$ and also for the L-C-R discharge with simulated value of the DR_0. In both cases it is seen clearly that a capacitor bank of voltage V_0 discharging into a constant resistance such as DR_0 will have a peak current I_{peak} approaching an asymptotic value of $I_{peak}=V_0/DR_0$ when the bank capacitance C_0 is increased to such large values that the value of $Z_0=(L_0/C_0)^{0.5} << DR_0$. Thus DR_0 causes current 'saturation'.

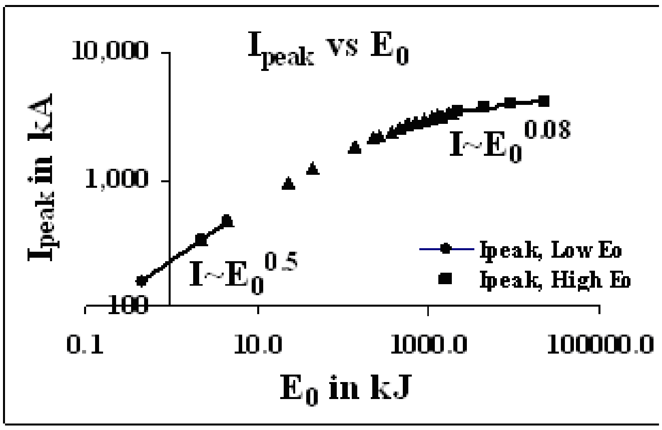

Figure. 16. I_{peak} vs E_0 on log-log scale, illustrating I_{peak} 'saturation' at large E_0

9.4. Deterioration in current scaling causes deterioration in neutron scaling

In Section 7.2 we had shown the following relationships between Y_n and I_{peak} and I_{pinch} as follows:

$$Y_n \sim I_{pinch}^{4.5} \tag{8}$$

$$Y_n \sim I_{peak}^{3.8} \tag{9}$$

Hence saturation of I_{peak} will lead to saturation of Y_n.

At this point we note that if we consider that only 0.7 of the total current takes part in driving the current sheet, as typically agreed upon from experimental observations, then there is a correction factor which reduces the axial dynamic resistance by some 40%. That would raise the asymptotic value of the current by some 40%; nevertheless there would still be 'saturation'.

Thus we have shown that current 'saturation' is inevitable as E_0 is increased to very large values by an increase in C_0, simply due to the dominance of the axial phase dynamic resistance. This makes the total circuit impedance tend towards an asymptotic value which approaches the dynamic resistance at infinite values of E_0. The 'saturation' of current inevitably leads to a 'saturation' of neutron yield. Thus the apparently observed neutron 'saturation' which is more accurately represented as a neutron scaling deterioration is inevitable because of the dynamic resistance. In line with current plasma focus terminology we will continue to refer to this scaling deterioration as 'saturation'. The above analysis applies to the Mather-type plasma focus. The Filippov-type plasma focus does not have a clearly defined axial phase. Instead it has a lift-off phase and an extended pre-pinch radial phase which determine the value of I_{peak}. During these phases the inductance of the Filippov discharge is changing, and the changing $L(t)$ will develop a dynamic resistance which will also have the same current 'saturation' effect as the Filippov bank capacitance becomes big enough.

The same scaling deterioration is also observed in the yield of Neon SXR (see Figure 13) and we expect for other radiation yields as well. The speed restrictions for a plasma focus operating in neon is not the same as that in deuterium. Nevertheless there is a speed window related to the optimum temperature window. This again requires fixing the dynamic resistance of the axial phase for the neon plasma focus within certain limits typically the dynamic resistance equivalent to an axial speed range of 5-8 cm per microsecond. This dynamic resistance and its interaction with the capacitor bank impedance as storage energy is increased is again the cause of the scaling deterioration.

9.5. Beyond presently observed neutron saturation regimes

Moreover the 'saturation' as observed in presently available data is due also to the fact that all tabulated machines operate in a narrow range of voltages of 15-50 kV. Only the SPEED machines, most notably SPEED II [59] operated at low hundreds of kV. No extensive data have been published from the SPEED machines. Moreover SPEED II, using Marx technology, has a large bank surge impedance of 50 mΩ which itself would limit the current. If we operate a range of such high voltage machines at a fixed high voltage, say 300 kV, with ever larger E_0 until the surge impedance becomes negligible due to the very large value of C_0. then the 'saturation' effect would still be there, but the level of 'saturation' would be proportional to the voltage. In this way we can go far above presently observed levels of neutron 'saturation'; moving the research, as it were into presently beyond-saturation regimes.

Could the technology be extended to 1MV? That would raise I_{peak} to beyond 15 MA and I_{pinch} to over 6 MA. Also multiple Blumleins at 1 MV, in parallel, could provide driver impedance of 100 mΩ, matching the radial phase dynamic resistance and provide fast rise currents peaking at 10 MA with I_{pinch} value of perhaps 5 MA. Bank energy would be several MJ. The push to higher currents may be combined with proven neutron yield enhancing methods such as doping deuterium with low % of krypton [60]. Further increase in pinch current might be by fast current injection near the start of the radial phase. This could be achieved with charged particle beams or by circuit manipulation such as current-stepping [11,61,62]. The Lee model is ideally suited for testing circuit manipulation schemes.

10. Neutron Scaling- Its relationship with the plasma focus properties

In Section 2 we had discussed the global scaling law for neutron yield as shown in Figure 1 which was compiled with data from experiments and numerical experiments. Figure 1 shows that whereas at energies up to tens of kJ the $Y_n \sim E_0^2$ scaling held, deterioration of this scaling became apparent above the low hundreds of kJ. This deteriorating trend worsened and tended towards $Y_n \sim E_0^{0.8}$ at tens of MJ. The global data of Figure 1 suggests that the apparently observed neutron saturation effect is overall not in significant variance with the deterioration of the scaling shown by the numerical experiments.

10.1. Relationship with plasma focus scaling properties

Now we link up this neutron scaling law deterioration and subsequent saturation with the scaling properties of the plasma focus discussed in Section 3. This scaling law deterioration and saturation is due to the constancy of the speed factor SF and energy density, as E_0 increases. The constancy of the axial speed or SF caused the deterioration of current scaling, requiring that the anode radius 'a' is not increased as much as it would have been increased if there were no deterioration. This implies that the size and duration of the focus pinch are also restricted by the scaling deterioration. Ultimately at high tens of MJ, I_{peak} saturates, the anode radius of the focus should not be increased anymore with E_0. The size and duration of the focus pinch no longer increase with E_0 and Y_n also saturates. We now have the complete picture.

We may consider the other effects such as the current limitation effect as inductance is reduced and the scaling laws of plasma focus for SXR yield. These are all related to the behaviour of the scaling properties and the interaction of these scaling properties, particularly the dynamic resistance with the capacitor bank impedance.

11. New Development-The 6-phase model- Instability phase fitted by anomalous resistance(s)

11.1. Low inductance plasma focus Type T1- Computed current trace well fitted to measured current trace using 5-phase model

The Lee code does not model the transition from Phase 4 to Phase 5. Nevertheless it has been found to be adequate for modelling all the well-known plasma focus with low static inductance L_0 [14-16,32,35,47,49] which we have fitted; in the sense that the computed current traces can be fitted to the measured current trace by adjustment of the model parameters f_m, f_c, f_{mr} and f_{cr}. This has been the case for the PF1000, PF400J, NX1, NX2, DPF78, Poseidon [14], FMPF1 [63], FN-II [49]. Some examples are shown in figures 17.

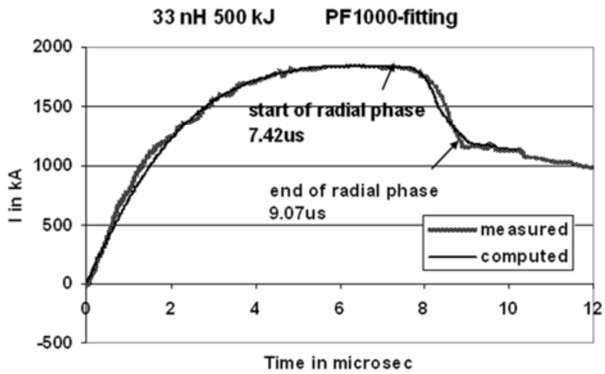

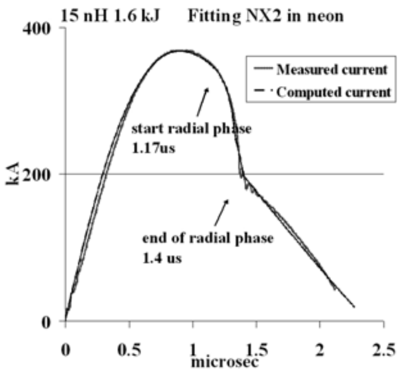

Figure 17a. PF1000 current traces- Good Fit

Figure 17b. NX2 current traces- Good fit

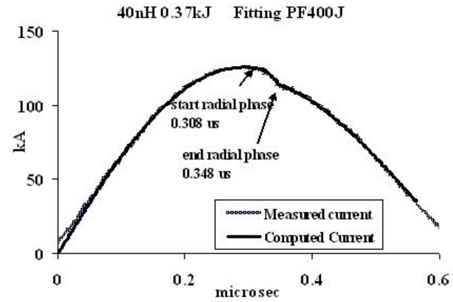

Figure 17c. Computed current trace of PF-400J fitted to the measured current trace.

11.2. High inductance plasma focus Type T2- Computed current trace cannot be fitted to measured current trace using 5-phase model

Amongst the well-published plasma focus devices only the UNU/ICTP PFF [14,16,25-27] which has relatively higher L_0 of 110 nH presented less certainty in the fitting. This was due to a very small computed current dip and a measured current dip that has always been masked by very large oscillations taken to be noise; although when operated in unusually low pressure regime, a clear discrepancy was noted between the computed and measured current trace [64].

Recently a current trace from the newly commissioned KSU DPF (Kansas State University Dense Plasma Focus) [65] which has an even higher L_0, was obtained by numerically integrating the output of a *dI/dt* coil. An analysis of the frequency response of the coil system and the DSO signal acquisition system showed that noise frequencies below 200 MHz were removed by the numerical integration. The resultant waveform is clean and clearly shows an extended current dip with good depth and duration (see figure 18, the darker trace).

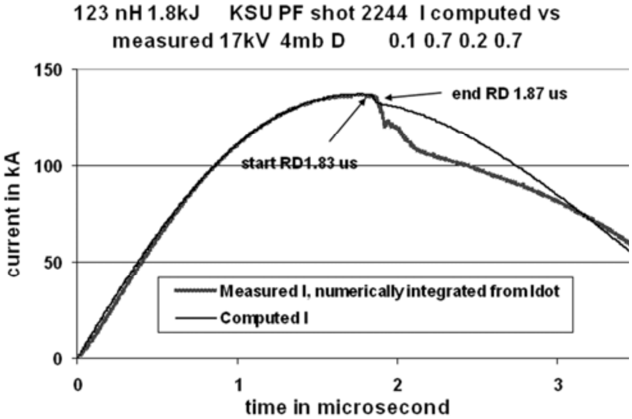

Figure 18. Computed current trace (lighter trace) with best attempt to fit to the measured current trace (darker trace).

Following the usual procedure of the Lee model code, an attempt was made to fit the computed current trace with the measured. The computed current trace has only a small dip as is characteristic of the computed current dip of a device with large static inductance L_0. All possible adjustments were made to the model parameters but the computed current dip could not be made to fit the whole measured current dip. The best fit is shown in figure 18; which shows that the computed dip does fit the first small part of the measured current dip. But the measured dip continues on in both depth and duration far beyond the computed dip.

11.3. Factors distinguishing the two types of plasma focus devices

The code models the electrodynamic situation using the slug model and a reflected shock for the radial phase, ending the radial phase in phase 4. Let's call the radial phase modeled in that manner as the REGULAR radial phase. This REGULAR radial phase, in increasing sharply the inductance of the system (constituting also a dynamic resistance [10,11]) causes a dip on the current trace. Call this the regular dip *RD*. At the end of the REGULAR radial phase experimental observations point to another phase [5,55,56], which we shall call phase 4a, (i.e. after phase 4, but before the final axial phase, called phase 5), of 'instabilities' manifesting in anomalous resistance. These effects would also extract energy from the magnetic field and hence produce further current dips. These effects are not modeled specifically in the code. Call this the extended current dip *ED*.

However it may be argued that as long as the model parameters can be stretched sufficiently to have the computed current dip agree with the measured current dip, then in a gross sense, the modelling is energetically and mass-wise equivalent to the physical situation. Then the resulting gross characteristics from the model would give a fair representation of the actual plasma properties, even though the model has not specifically modeled *ED*. In other words *RD* is able to be stretched to also model *ED*, with equivalent energetics and mass implications. Whether *RD* can be stretched sufficiently to cover *ED* depends on the relative sizes of the two effects. If *RD* is already a big dip, then this effect may dominate and it is more likely that *RD* may be stretched sufficiently to cover the less prominent *ED*. If *RD* is only a miniscule dip and *ED* is a big dip, then it is unlikely that the *RD* can be stretched enough to encompass the *ED*.

We attempt to establish criteria for discriminating the types. Noting that generally a plasma focus with small L_0, for example the PF1000 with L_0=33 nH, exhibits a large computed *RD* (see figure 16) whereas a plasma focus with a large L_0, for example the KSU PF with L_0=123 nH, exhibits a small computed *RD* (see figure 18) we suspect that it has something to do with the inductance L_0, or the ratio of L_0 with various inductances inherent in the system. We carried out several series of numerical experiments with various configurations similar to existing plasma focus devices, varying the value of L_0 in each series and looking at the effect on remnant energies at the end of the *RD*. Some interesting conclusions may be drawn from a tabulation, such as in Table 7.

Table 7. Classification of Plasma Focus Machines (D_2 operation).

PF name	L_0 (nH)	C_0 (F)	I_{peak} (kA)	R_L	R_{EL}	*RD* dip (%)	Type
Poseidon	17.7	156	3205	0.9	2.5	32	*T1*
PF1000	33.5	1332	1845	1	1.6	34	*T*1
DPF78	55	17.2	869	4.1	12.8	11	*T1*
FN-II	75	7.5	309	4.3	8.5	10	*T1*
FMPF1	31	2.4	81	6.9	8.6	14.5	*T1*
PF-400J	40	1	126	8.8	17.3	8	*T1*
UNUICTP	110	30	163	16.7	29.5	1.9	*T2*
KSU	123	12.5	137	21.4	40	1.5	*T2*

We considered the inductance ratio $R_L=(L_0+L_a)/L_{pinch}$ where L_{pinch} is the inductance of the focus pinch at the end of the REGULAR radial phase, L_0 the bank static inductance and L_a the inductance of the axial part of the focus tube. We also considered the remnant energy ratio $R_{EL}=(E_{L0}+E_{La})/E_{Lpinch}$ where E_{L0}= energy stored in L_0 at end of the *RD*, E_{La}=energy stored in L_a at end of the *RD* and E_{Lpinch}=energy stored inductively in the pinch at end of *RD*.
Computing the values of these two quantities for PF1000, Poseidon, DPF78, NX2, PF400J, FMPF-1, FNII and UNU/ICTPPFF and KSU PF, we have a range of devices from very big (MJ) to rather small (sub kJ) of which we have well documented fittings. These are shown in Table 7 for operation in D_2. For other gases there are not many readily available examples. We are able to compile Table 8 for operation in Ne.

Table 8. Classification of Plasma Focus Machines (Ne operation).

PF name	L_0 (nH)	C_0 (F)	I_{peak} (kA)	R_L	R_{EL}	*RD* dip (%)	Type
NX2 Ne	20	28	322	1.5	2.6	19	*T1*
UNUICTP Ne	110	30	178	15	26	2.5	*T2*

Generally we see the trend that the smaller is the ratio R_L, the bigger is the regular current dip (*RD*). When this ratio is large (primarily due to a large L_0 in the numerator), like in the case of KSU PF, the REGULAR radial phase RD is miniscule. Likewise, the trend is also observed for the ratio R_{EL}. The smaller this energy ratio, the bigger is the current dip.
On the basis of these two ratios we have divided the plasma focus devices in Tables 7 and 8 into two types: T1 and T2. Type T1 are for plasma focus devices with relatively small L_0 with large RD's and with relatively small ratios R_L and R_{EL}. These T1 focus devices are well-fitted using the Lee model code. The computed current traces (with radial phase computed only as a regular dip RD) are well-fitted to the whole measured current trace. Type *T2* are for plasma focus devices with relatively large L_0 with small *RD*'s and with relatively large ratios of R_L and R_{EL}. These *T2* focus devices are not well-fitted using the Lee model code. The computed current trace shows only a small dip which is fitted to the first portion of the measured current dip; but the measured current dip has an extended portion which is not well-fitted using the 5-phase Lee model code.
Next we note that the magnetic energy density per unit mass at the start of the radial phase is the same across the whole range of devices [6]. Thus *T1* with a big *RD* drops the current a lot and

strongly depletes the magnetic energy per unit mass at the end of the RD, leading to a small *ED*. Consequently *T1* are completely fitted using a model that computes only the *RD*, stretching the model parameters until the large *RD* covers also the small *ED*. Conversely a *T2* plasma focus has a small *RD*, consequently a large *ED* and cannot be completely fitted with the computed *RD*. Thus a big RD drops the current a lot and strongly depletes the magnetic energy per unit mass at the end of the REGULAR radial phase. Hence a device with small R_L produces a big RD and ends up with relatively less energy per unit mass at the end of the REGULAR phase when compared to a device with a big value of R_L. Therefore a big *RD* generally tends to lead to a small *ED*; whereas a small *RD* is more conducive to lead to a larger *ED*.
From the above we may surmised that T1 plasma focus has a big *RD*, consequently a small *ED* and hence can be completely fitted using a model that computes only the *RD*, which is able to stretch its *RD* by stretching the model parameters until the large *RD* covers also the small *ED*. Moreover energetically and mass-wise the fitting is correct. On the other hand *T2* plasma focus has a small *RD*, consequently a large *ED*. *T*2 plasma focus cannot be completely fitted with the *RD* computed from the code, no matter how the model parameters are stretched. To fit the computed current trace to the measured current for *T2*, a phase 4a needs to be included into the model in order to progress the current dip beyond the small *RD* into the large *ED* part of the current dip.

11.4. The anomalus resistance term in the 6-phase Lee Model

It is generally accepted [5] that after the regular dynamic phases ending in the formation of the plasma focus pinch, at the end of the pinch the system becomes unstable, develops a high 'anomalous' resistivity and breaks up. The overall processes to start this instability takes an exceedingly short time, the experimental observations indicate that the breakup time is far shorter than the 'regular' radial phases. This is evident for example in streak photographs which show that the break up time is less than the duration of the pinch. For example for a small focus of around 10 kJ the breakup time has been measured [66] as 30ns after a duration of some 80 ns for the radial inward shock and reflected shock phases. There appears to be large number of competing instability processes [5], among which are some with exceedingly short time scales. Hence it appears reasonable to assume that the speed at which the plasma can convert the remnant inductive energy into anomalously resistive energy is ultimately limited by the time scales of the gross electrical components which have to supply the energy for the break-up processes.
From a careful study of measured waveforms of current and voltages, various sources have reported that the plasma anomalous resistive voltages are consistent with an 'anomalous' resistance of the order of 1 Ω [5,66]. Hence the (1/e) time scale (which is L/R) of current is estimated as 10 ns per 10 nH of inductance (L_0+L_a+L_{pinch}); that is the time it takes the current to drop to some 36% limited by the lumped components of the circuit. Because inductive energy is proportional to I^2, this is also the time it would take for the inductive energy to drop to some 14%. On the other hand, the time it takes for inductive energy to drop to 55% $(\exp[-0.3])^2$ is some 3 ns per 10 nH. For a low L_0 (20-30 nH) plasma focus with this quantity of inductance (L_0+L_a+L_{pinch}) of around 40 nH this range of time (for inductive energy drop to 14% to 55%) is of the order of 12-40 ns. On the other hand for a high L_0 plasma focus with L_0=120 nH and the total inductance being 130 nH, this 14% to 55% inductive energy drop range could be some 40-130 ns. Thus for a low L_0 system assuming a range of inductive energy drop down to 14 to 55 %, we may estimate a relatively small *ED* region with small depth and timescale of the order of 12 to 40ns. Whereas for a high L_0 system we expect a relatively high dip *ED* region with time scales of the order of 40-130 ns.

Therefore a low L_0 system would have a small (in depth and in time) *ED* which can easily be merged into the larger (in depth and in time) *RD*; the whole current dip being capable of being treated as just the *RD*. On the other hand the high L_0 system would have an *E*D which is large (in both depth and time) when compared with the *RD*; hence the *ED* has to be separately treated by modelling a phase 4a.

One way to simulate the current *ED* is to assign the phase 4a period with an anomalous resistance term such as:

$$R=R_0[exp(-t/t_2)-exp(-t/t_1)] \qquad (10)$$

where R_0 is of the order of 1Ω, t_1 is a characteristic time representative of the rise time of the anomalous resistance and t_2 is characteristic of the fall time of the anomalous resistance (Figure 19).

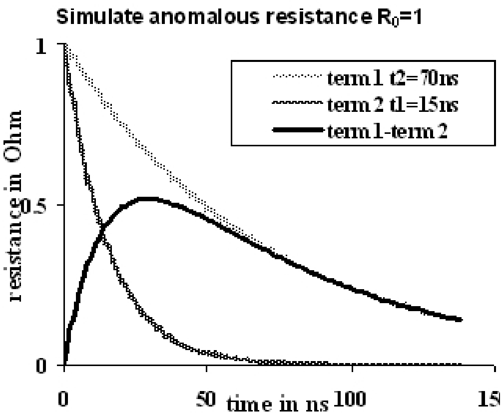

Figure 19. Simulating anomalous resistance.

11.5. The first result of the 6-phase model

We have applied this technique to the KSU current waveform (Figure 18). We note that the computed *RD* only agrees with a small part of the measured current dip and does not follow the measured current dip which goes on to an *ED*. Following that first current dip in this particular case the dip continues in a second portion which is almost flat then followed by a third section which is less steep than the first dip but of slightly longer duration. We applied a resistance term to each of the 3 sections. We adjusted the parameters R_0, t_2 and t_1 for each of the section as well as a fraction (*endfraction*) which terminates the term. The fitted parameters are as follows:

Table 9. Anomalous resistances used for the fitting.

	R_0 (Ω)	T_2(ns)	T_1 (ns)	*endfraction*
Dip 1 *ED*	1.0	70	15	0.53
Dip 2	0.2	70	40	0.4
Dip 3	0.5	70	25	1.0

With these parameters it is found that the computed current dip now fits the measured current dip all the way to the end of the current dip. The fitting has involved the fitting of the *RD*, followed by the *ED* of the first dip; then follow the second and third dips treated as *ED*'s, each requiring a separate anomalous resistance function.

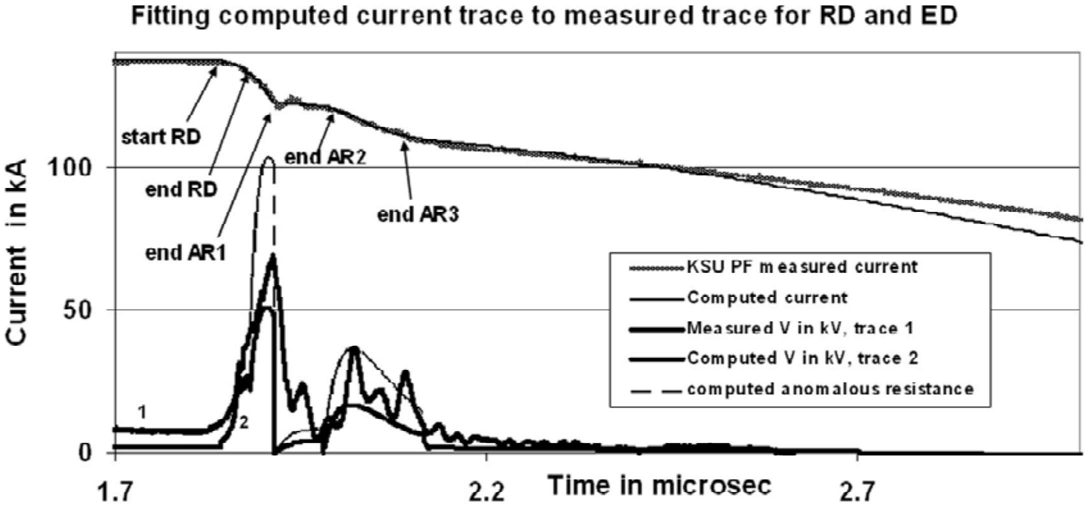

Figure 20. Computed Current (dip region only and expanded to see details) fitted to measured current with inclusion of Phase 4a.

The resistance functions used for the fitting are also shown in Figure 20 (dashed trace, with the resistance values magnified 200 times in order to be visible on the scale of Figure 20). The computed voltage waveform is also shown (trace labeled 2) compared with the measured voltage waveform (trace labeled 1). The correspondence of the computed voltage waveform and the measured is seen clearly [67].

12. Conclusion

This paper has reviewed the extensive and systematic numerical experiments which have been used to uncover new insights into plasma focus fusion devices including the following. A plasma current limitation effect was unexpectedly found, as the static inductance of any focus device is reduced towards very small values. Scaling laws of neutron yield and soft x-ray yield as functions of storage energies, circuit peak current as well as plasma pinch current, were developed over wider range of parameters than attempted previously. This paper has reviewed the global scaling law for neutron yield as a function of storage energy. First, the scaling deterioration and eventual ‘saturation’ of circuit current are ascribed to the energy density constancy manifested in the form of a constancy in dynamic resistance of the axial phase. Second, the deterioration of current scaling implies that the anode radius ‘a’ is not increased as much as it would have been if there were no deterioration. Third, this implies that the size and duration of the focus pinch are also restricted by the scaling deterioration. Ultimately at high tens of MJ, I_{peak} saturates, the anode radius of the focus should not be increased anymore with E_0, the size and duration of the focus pinch no longer increase with E_0.

The restriction on the plasma pinch size and duration has a corresponding effect on the neutron yield Y_n. The neutron yield Y_n scales with E_0^2 at low energies up to tens of kJ, begins to exhibit scaling deterioration around low hundreds of kJ and approaches ‘saturation’ at high tens of MJ.

In this manner this paper has connected the global scaling laws for the current and the neutron yield to the scaling properties of the plasma focus. This more complete picture will facilitate deeper understanding and the further development of the plasma focus as a fusion device.

Through these numerical experiments, the cause of neutron ‘saturation’ as device storage energy is increased is found to be the axial phase ‘dynamic resistance’. With the fundamental cause discovered, it is suggested that beyond ‘present saturation’ regimes may be reached by going to higher voltages, and using plasma current enhancement techniques such as current-steps.

Finally a brief discussion is made on the latest development to the Lee Model code, extending it into a 6^{th} phase; the so-called phase 4a which links the end of the pinch phase 4 to the large column axial phase 5. This new development classifies plasma focus into T1 and T2. The T1 devices (with low L_0) have all been fitted well using the 5-phase Lee Model code. The T2 devices are the high inductance (high L_0) type for which the 5-phase model is inadequate. The post-pinch instabilities phase is modeled using an equivalent anomalous resistance which then enables the T2 measured current waveform to be fitted to the measured current waveform in the portion beyond the RD (regular dip) extending the ED (extended dip). The fitting of the anomalous resistance(s) thus results in quantitative experimental data for the instability phase. The anomalous resistance, in effect measured by this method will provide quantitative information for understanding the instabilities.
It is expected that numerical experiments will continue to play a major role complementing and even guiding laboratory measurements and practices. The ground-breaking insights thus gained will completely open up the directions of plasma focus fusion research.

References

[1] ITER website**.** **http://www.iter.org**
[2] Sing Lee. Nuclear Fusion and the Plasma Focus. Invited paper Tubav Conferences: Nuclear & Renewable Energy Sources Ankara, Turkey, 28 & 29 September 2009. Procs:pg 9-18
[3] D E Potter Numerical Studies of the Plasma Focus Phys. Fluids **14**, 1911-1914 (1971)
[4] Leopoldo Soto. New trends and future perspectives on plasma focus research 2005 *Plasma Phys. Control. Fusion* **47** A361
[5] Bernard A., Bruzzone H., Choi P., Chuaqui H., Gribkov V., Herrera J., Hirano K., Krejci A., Lee S., Luo C.et al Scientific Status of Plasma focus Research. *Moscow J Physical Society,* 1998*,* **8***,* 93-170.
[6] Lee S. and Serban A., "Dimensions and lifetime of the plasma focus pinch," *IEEE Trans. Plasma Sci.*, 1996**,** ***24***, no. 3, pp. 1101–1105, Jun. 1996.
[7] Lee S, "Scaling of the Plasma Focus-Viewpoint from Dynamics" International Plasma Focus Symposium, Kudowa, Poland July 1998
[8] Lee, S. Characterising the Plasma Focus Pinch and Speed Enhancing the Neutron Yield. In: First Cairo Conference on Plasma Physics & Applications. 11-15 October 2004. International Cooperation Bilateral Seminars (Vol **34**). Forschungszentrum Juelich GmbH, Juelich, Germany, pp. 27-33. ISBN 3-89336-374-2
[9] Rapp H. *Phys Lett A*, 1973, ***43A****,* 420-422.
[10] Lee S., "Current and neutron scaling for Megajoule plasma focus machines," *Plasma Phys. Control. Fusion*, 2008, ***50***, no. 10, p. 105 005 (14pp).
[11] Lee S. "Neutron Yield Saturation in Plasma Focus-A fundamental cause" *APPLIED PHYSICS LETTERS*, 2009, ***95***, 151503 published online 15 October 2009
[12] Lee, S.; Tou, T. Y.; Moo, S. P.; Eissa, M. A.; Gholap, A. V.; Kwek, K. H.; Mulyodrono, S.; Smith, A. J.; Suryadi, S.; Usada, W.;. Zakaullah, M. A simple facility for the teaching of plasma dynamics and plasma nuclear fusion. *Amer. J. Phys.* 1988, ***56****,* no. 1, 62–68.
[13] Gribkov V. A., Banaszak A., Bienkowska B., Dubrovsky A. V, Ivanova-Stanik I., Jakubowski L., Karpinski L., Miklaszewski R. A., Paduch M., Sadowski M. J., Scholz M., Szydlowski A., and Tomaszewski K., Plasma dynamics in the PF-1000 device under fullscale energy storage: II. Fast electron and ion characteristics versus neutron emission parameters and gun optimization perspectives, *J. Phys. D,Appl. Phys.*, 2007, ***40***, no. 12, pp. 3592–3607
[14] Web-site: http://www.intimal.edu.my/school/fas/UFLF/

[15] Soto L., Silva P., Moreno J., Silvester G., Zambra, M., Pavez, C., Altamirano L., Bruzzone H., , Barbaglia, M., Sidelnikov Y., & Kies, W. Brazilian J Phys 34, 1814 (2004)
[16] Lee S. Radiative Dense Plasma Focus Computation Package: RADPF, 2010
http://www.plasmafocus.net
http://www.plasmafocus.net/IPFS/modelpackage/File1RADPF.htm
http://www.plasmafocus.net/IPFS/modelpackage/File2Theory.pdf
http://www.plasmafocus.net/IPFS/modelpackage/UPF.htm
[17] Lee, S. Plasma focus model yielding trajectory and structure. In *Radiations in Plasmas*, McNamara, B., Ed.; World Scientific, Singapore: 1984; Volume II, pp. 978–987.
[18] Tou, T. Y.; Lee, S.; Kwek, K. H. Non perturbing plasma focus measurements in the run-down phase. *IEEE Trans. Plasma Sci.* **1989**, *17*, no. 2, 311–315.
[19] Lee, S. A sequential plasma focus. *IEEE Trans. Plasma Sci.* 1991**,** ***19***, no.5, 912–919.
[20] Jalil bin Ali. *Development and studies of a small plasma focus*, Ph.D. Dissertation; Universiti Teknologi Malaysia, Malaysia, 1990**.**
[21] Potter, D. E. The formation of high-density z-pinches. *Nucl. Fusion.* 1978**,** ***18***, 813–823.
[22] Liu M., "Soft X-rays from compact plasma focus," Ph.D. dissertation, NIE, Nanyang Technological Univ., Singapore, 2006. ICTP Open Access Archive. [Online]. Available: http://eprints.ictp.it/327/
[23] Bing S., "Plasma dynamics and X-ray emission of the plasma focus," Ph.D. dissertation, NIE, Nanyang Technological Univ., Singapore, 2000. ICTP Open Access Archive. [Online]. Available: http://eprints.ictp.it/99/
[24] Serban A. and Lee S., "Experiments on speed-enhanced neutron yield from a small plasma focus," *J. Plasma Phys.*, 1998, ***60***, no. 1, pt. 1, pp. 3–15, Aug. 1998.
[25] Liu M.H., Feng X.P., S. V. Springham, and Lee S., "Soft X-ray measurement in a small plasma focus operated in neon," *IEEE Trans. Plasma Sci.*, 1998, ***26***, no. 2, pp. 135–140.
[26] Lee S., in *Twelve Years of UNU/ICTP PFF—A Review*. Trieste, Italy: Abdus Salam ICTP, 1998, pp. 5–34. IC/ 98/ 231, ICTP Open Access Archive. [Online]. Available: http://eprints.ictp.it/31/
[27] Springham S. V., Lee S., and Rafique M. S., "Correlated deuteron energy spectra and neutron yield for a 3 kJ plasma focus," *Plasma Phys. Control. Fusion*, 2000, **42***,* no. 10, pp. 1023–1032.
[28] Lee S., 2000–2007. [Online]. Available: http://ckplee.home.nie.edu.sg/plasmaphysics/
[29] Lee S., *ICTP Open Access Archive*, 2005. [Online]. Available: http://eprints.ictp.it/85/
[30] Mohammadi M. A., Sobhanian S., Wong C. S., Lee S., Lee P., and Rawat R. S., "The effect of anode shape on neon soft X-ray emissions and current sheath configuration in plasma focus device," *J. Phys. D, Appl. Phys.*, 2009, ***42***, no. 4, 045 203 (10pp).
[31] Wong D., Lee P., Zhang T., Patran A., Tan T. L., Rawat R. S., and Lee S., "An improved radiative plasma focus model calibrated for neon filled NX2 using a tapered anode," *Plasma Sources Sci. Technol.*, 2007. ***16***, no. 1, pp. 116–123.
[32] Lee S., P. Lee, Zhang G., Feng X., Gribkov V. A., Liu M., Serban A., and Wong T., "High rep rate high performance plasma focus as a powerful radiation source," *IEEE Trans. Plasma Sci.*, 1998, ***26***, no. 4, pp. 1119–1126.
[33] Bogolyubov E. P., Bochkov V. D., Veretennikov V. A., Vekhoreva L. T., Gribkov V. A., Dubrovskii A. V., Ivanov Y. P., Isakov A. I, Krokhin O. N., Lee P., Lee S., Nikulin V. Y., Serban A., Silin P. V., Feng X., and Zhang G. X., "A powerful soft X-ray source for X-ray lithography based on plasma focusing," *Phys. Scr.*, 1998, ***57***, no. 4, pp. 488–494.
[34] Siahpoush V., Tafreshi M. A., Sobhanian S., and Khorram S., "Adaptation of Sing Lee's model to the Filippov type plasma focus geometry," *Plasma Phys. Control. Fusion*, 2005, ***47***, no. 7, pp. 1065–1075.

[35] Lee S. and Saw S. H., "Neutron scaling laws from numerical experiments," *J. Fusion Energy*, 2008, ***27***, no. 4, pp. 292–295.
[36] Lee S., Saw S. H., Lee P. C. K., Rawat R.S., and Schmidt H., "Computing plasma focus pinch current from total current measurement," *Appl. Phys. Lett.*, 2008, ***92***, no. 11, p. 111 501.
[37] Lee S. and Saw S. H., "Pinch current limitation effect in plasma focus," *Appl. Phys. Lett.*, 2008, ***92***, no. 2, p. 021 503.
[38] Lee S., Lee P., Saw S. H., and Rawat R. S., "Numerical experiments on plasma focus pinch current limitation," *Plasma Phys. Control. Fusion*, 2008, ***50***, no. 6, 065 012 (8pp).
[39] Internet Workshop on Plasma Focus Numerical Experiments (IPFS-IBC1) 14 April-19 May 2008 http://www.plasmafocus.net/IPFS/Papers/IWPCAkeynote2ResultsofInternet-basedWorkshop.doc
[40] Akel M., Al-Hawat Sh., Lee S. "Pinch Current and Soft x-ray yield limitation by numerical experiments on Nitrogen Plasma Focus". *J Fusion Energy* DOI 10.1007/s10894-009-9238-6. First online 21 August 2009
[41] Saw S. H. and Lee S. " Scaling laws for plasma focus machines from numerical experiments". Invited paper: IWPDA, Singapore 2&3 July 2009
[42] Lee S. Diagnostics and Insights from Current waveform and Modelling of Plasma Focus. Keynote address: IWPDA, Singapore 2-July 2009
[43] Saw S. H. and Lee S. "Scaling the plasma focus for fusion energy considerations". Tubav Conferences: Nuclear & Renewable Energy Sources, Ankara, Turkey, 28 & 29 September 2009.
[44] Lee S., Saw S. H., Lee P. & Rawat R. S., "Numerical Experiments on Neon plasma focus soft x-rays scaling", *Plasma Physics and Controlled Fusion*, 2009, ***51***, 105013 (8pp).
[45] Akel M., Al-Hawat Sh., Lee S. "Numerical Experiments on Soft X-ray Emission Optimization of Nitrogen Plasma in 3 kJ Plasma Focus SY-1 Using Modified Lee Model", *J Fusion Energy* DOI 10.1007/s10894-009-9203-4 First online, May 19, 2009.
[46] M. Akel, Sh. Al-Hawat, S. H. Saw and S. Lee. Numerical Experiments on Oxygen Soft X-Ray Emissions from Low Energy Plasma Focus Using Lee Model. Journal of Fusion Energy DOI 10.1007/s10894-009-9262-6 First online 22 November 2009
[47] Lee S., Rawat R. S., Lee P., S H Saw S. H., Soft x-ray yield from NX2 plasma focus, *JOURNAL OF APPLIED PHYSICS*, 2009, ***106***, 023309.
[48] Saw S. H., Lee P. C. K., Rawat R. S. & Lee S. 2009 'Optimizing UNU/ICTP PFF Plasma Focus for Neon Soft X-ray Operation' *IEEE Trans on Plasma Sc*, 2009, ***37***, 1276-1282.
[49] Lee S., Saw S. H., Soto L., Moo S. P., Springham S. V., Numerical experiments on plasma focus neutron yield versus pressure compared with laboratory experiments, *Plasma Phys. Control. Fusion*, **2009**, ***51*** 075006 (11pp)
[50] Chow S P, Lee S and Tan B C 1972 *J. of Plasma Phys*., UK, **8**: 21-31.
[51] Sing Lee amd Sor Heoh Saw "Numerical Experiments Providing New Insights into Plasma Focus Fusion Devices" *Energies* 2010, ***3***, 711-737; doi:10.3390/en3040711
[52] Huba J D 2006 Plasma Formulary page 44 http://wwwppd.nrl.navy.mil/nrlformulary/NRL_FORMULARY_07.pdf
[53] Gates D C 1978 Proceedings of the IInd Int Conference on Energy Storage, Compression and Switching, Venice, **2**, 3239 (Plenum Press, New York, 1983).
[54] Filippov N V, Filippova T I, Khutoretskaia I V, Mialton V V and Vinogradov V P, "Megajoule scale plasma focus as efficient X-ray source," Physics Letters A Vol 211, Issue 3, 168-171, 1996

[55] Kraus V. I. “Progress in plasma focus research and applications”. 33rd EPS Conference on Plasma Physics, Rome, June 20, 2006 *Plasma Phys. Control. Fusion, 2006, **48**,* B221-B229.
[56] Scholz M., Report at the ICDMP Meeting, ICDMP, Warsaw, Poland, November 2007
[57] W Kies in *Laser and Plasma Technology*, Procs of Second Tropical College Ed by S Lee et al, World Scientific, Singapore ISBN 9971-50-767-6 (1988) p86-137
[58] H Herold in *Laser and Plasma Technology*, Procs of Third Tropical College Ed by C S Wong et al, World Scientific, Singapore ISBN 981-02-0168-0 (1990) p21-45
[59] G. Decker, W. Kies, R. Nadolny, P. Röwekamp, F. Schmitz, G. Ziethen, K. N. Koshelev, and Yu. V. Sidelnikov, Plasma Sources Sci. Technol. **5**, 112 (1996)
[60] Rishi Verma, P. Lee, S. Lee, S. V. Springham, T. L. Tan, R. S. Rawat, and M. Krishnan “Order of magnitude enhancement in neutron emission with deuterium-krypton admixture operation in miniature plasma focus device” Appl. Phys. Lett. **93**, 101501 (2008); doi:10.1063/1.2979683 (*3 pages*)
[61] Saw S H, “Experimental studies of a current-stepped pinch.” PhD Thesis Universiti Malaya, Malaysia, 1991.
[62] Lee S “A current-stepping technique to enhance pinch compression” J *Phys D: Appl Phys* **17**, 733-739. 1984
[63] Rishi V, Rawat R S, Lee P, Lee S, Springham S V, Tan T L and Krishnan M 2009 *Phys Letts A* **373** 2568–2571
[64] Yap S L, Lee S H, Lim L K and Wong C S. Dynamics of a Small Plasma Focus Device. Procs International Workshop on Plasma Computations and Applications (IWPCA2008) 14-15 July 2008 ISSN 165-0284. INTI Publishing House Sdn Bhd, Malaysia. Ed: Saw Sor Heoh et al p51-54
[65] A. Abdou, R. Verma, R. S. Rawat, P. L. Choon Keat, S. V. Springham, S. Lee “Characterization of Kansas State University Dense Plasma Focus as a Multi-Radiation Source”, 37th IEEE International Conference on Plasma Science ICOPS, Norfolk, VA, USA, June 20-24 2010
[66] Tou T Y “Pinch Radius Ratio of the Plasma Focus” Ph D thesis, Universiti Malaya, Kuala Lumpur, Malaysia, 1986
[67] S Lee, S H Saw, A E Abdou and H Torreblanca**.** Characterizing plasma focus devices- role of the static inductance- instability phase fitted by anomalous resistances-submitted for publication